Theoretical exploration of femtosecond multi-state nuclear dynamics of small clusters

Michael Hartmann, Jiří Pittner, and Vlasta Bonačić-Koutecký
Walther-Nernst-Institut für Physikalische und Theoretische Chemie, Humboldt-Universität zu Berlin, Bunsenstraße 1, D-10117 Berlin, Germany

Andreas Heidenreich and Joshua Jortner
School of Chemistry, Tel Aviv University, Tel Aviv 69978, Israel

(Received 17 October 1997; accepted 17 November 1997)

We investigate ultrafast multi-state nuclear dynamics in a triatomic cluster. In particular, we explore how the intracluster nuclear dynamics of the $Ag_3^-/Ag_3/Ag_3^+$ system is reflected in the femtosecond pump-probe negative ion-to neutral-to positive ion (NENEPO) signals. The nuclear dynamics is based on classical trajectories on the ground electronic adiabatic state potential hypersurfaces obtained from accurate *ab initio* quantum chemistry calculations. The nuclear dynamics of Ag_3 initiated from the linear transition state involves distinct sequential processes of configurational relaxation to the triangular configuration, intracluster collisions, and the onset of IVR, resonant, and dissipative IVR, and vibrational equilibration. We determined the timescales for these processes and discussed their dependence on the initial cluster temperature. The Wigner representation of the density matrix was utilized to simulate the NENEPO-zero kinetic energy (NENEPO-ZEKE) signal and the total (integrated over the photoelectron energy) NENEPO signal. We show how geometrical change, completion of IVR and vibrational coherence effects can be identified in the NENEPO signals. A comparison of the calculated NENEPO signals with the available experimental data is presented. © *1998 American Institute of Physics.* [S0021-9606(98)00708-9]

I. INTRODUCTION

Remarkable progress in the exploration of femtosecond intramolecular, cluster, and condensed phase dynamics on the timescale of nuclear motion[1–3] stems from concurrent progress in theory and experiment. The advent and utilization of femtosecond lasers allows for a real-time interrogation of intramolecular and intermolecular electronic and nuclear dynamics during chemical transformations.[1–3] The theory and simulations of radiationless processes,[4] wave packet dynamics,[5] coherence effects,[5] cluster dynamic size effects,[6] nonadiabatic and adiabatic condensed phase dynamics,[4] and nonlinear optical interactions[7] provide the conceptual framework for ultrafast chemical and biophysical dynamics.

A central application of ultrafast dynamics pertains to configurational changes and internal vibrational energy redistribution in vertically excited or ionized electronic-vibrational states of polyatomic molecules and clusters. In particular, clusters are of considerable interest in this context because of several reasons.[6,8,9] First, clusters constitute finite systems where the number of degrees of freedom and the density of states can be continuously varied with changing the cluster size.[6,8] Second, the nuclear dynamics of clusters allows for the separation of time scales.[9] Third, dynamic cluster size effects allow for the investigation of the ''transition'' from resonant dynamics to dissipative dynamics with increasing the cluster size.[10] Bridging between cluster (and molecular) dynamics and the fundamental chemistry, exploration of nuclear dynamics triggered by the vertical electronical-vibrational excitation or ionization pertains to transition state spectroscopy and dynamics, providing real-time interrogation of the transition state of chemical reactions.[11–19] The underlying idea involves the preparation of a transition state of a chemical reaction by the optical excitation of a stable collision complex in a nonequilibrium nuclear configuration, probing its temporal evolution by laser-induced fluorescence, photoelectron spectroscopy, or resonance enhanced multiphoton ionization. This approach is pioneered by Zewail and his colleagues for bimolecular reactions of alkali halides, mercury halides, and other systems.[11–13] In another approach advanced by Neumark,[14–16] transition states were generated by the vertical photodetachment of stable negative ions, where the ground state is characterized by a geometry close to that of the transition state of the corresponding neutral species. Related studies by Lineberger and his colleagues[17–19] demonstrated that vertical photodetachment of some negative organic ions can result in transition states for intramolecular isomerization of the neutral species. Wolf *et al.*[20] advanced a pioneering application of the vertical one-photon photodetachment technique to prepare a transition state of a triatomic molecule, which constituted a metal trimer, and its subsequent interrogation by a two-photon ionization. The so-called NENEPO (negative ion-to neutral-to positive ion) pump-probe femtosecond spectroscopy was applied to explore the nuclear dynamics of Ag_3.[20] In these experiments a transient linear Ag_3 cluster in its ground electronic state ($^2\Sigma_u^+$) was prepared by one-photon detachment of linear Ag_3^- ($^1\Sigma_g^+$) and its temporal evolution from linear Ag_3 ($^2\Sigma_u^+$) to triangular Ag_3 ($^2B_2$) structure was interrogated by

a delayed ionizing pulse via two-photon ionization. In this experiment[20] and subsequent studies by Leisner and Wöste,[21] the one-photon photodetachment energy was varied in the range 2.95–3.18 eV, while the two-photon interrogation pulse energy was varied in the range 5.90–6.36 eV. The work of Leisner, Wöste, Berry, and their colleagues[20,21] triggered theoretical analysis of the time dependence of the ionization potential of Ag_3 induced by structural response[22,23] and of pump-probe NENEPO dynamics of Ag_3^-,[24] and of $FeCO^-$.[25] A recent extension of the experimental study of Ag_3^- by the NENEPO pump-probe method, utilizing two-color excitation and interrogation by sensitive ion and electron detection, was presented by Lineberger *et al.*[26]

In this paper we present a theoretical study of the NENEPO femtosecond pump-probe signals and of the underlying nuclear dynamics of the Ag_3^-, Ag_3, and Ag_3^+ system, which can be considered as an important test case for theoretical concepts for the study of intracluster (intramolecular) dynamics in finite systems. A preliminary report of our work was already presented.[24] We have utilized the Wigner representation of the density matrix introduced by Li, Fang, and Martens[27] to simulate the pump-probe signal, requiring classical molecular dynamics trajectory calculations. The basis for our simulations are precomputed grids of the three potential energy hypersurfaces, which we have obtained from high quality *ab initio* configuration interaction (CI) and coupled cluster quantum chemistry calculations. The structures of the stable neutral and charged Ag_n $(n=2-9)$ clusters, as well as ionization potentials (IP) and vertical detachment energies (VDE), were already available from the previous work of Bonačić-Koutecký *et al.*[28,29] It is imperative to emphasize that critical scrutiny of concepts and information for intracluster (intramolecular) dynamics requires the use of accurate potential energy surfaces. From our semiclassical femtosecond pump-probe simulations for the multi-state nuclear dynamics information was inferred on the nuclear dynamics of Ag_3, which involves configurational changes, intracluster (intramolecular) collisions, intracluster vibrational energy redistribution (IVR),[1,30,31] and vibrational coherence effects.[5]

Our paper is organized as follows. In Sec. II we describe the Wigner representation of the density matrix for calculating the pump-probe signals. The simulated pump-probe signals are presented in Sec. V, together with an analysis of the interrelation between the temporal profile of the signals and the underlying nuclear dynamics. A comparison between simulated and experimental[20] NENEPO signals will be presented. The basis for this analysis is provided in Secs. III and IV. Specifically, in Sec. III we shall present the ground state potential energy surfaces (PES) of the Ag_3^-, Ag_3, and Ag_3^+ system and characterize their properties. In Sec. IV we address the nuclear relaxation dynamics of the neutral Ag_3 in its nonequilibrium state prepared by the pump excitation. The conclusions (Sec. VI) contain a summary and comparison of the simulated and experimental timescales of the dynamical processes in the Ag_3, as well as the interpretation of the pump-probe signals.

II. FEMTOSECOND PUMP-PROBE SIGNALS BASED ON SEMI-CLASSICAL MULTI-STATE NUCLEAR DYNAMICS

For the exploration of the time evolution of the molecular system after excitation by the electromagnetic field, we shall use the Wigner representation of the density matrix.[7,32] This approach is characterized by the conceptual simplicity of classical mechanics and the ability to describe approximatively quantum phenomena such as optical transitions. In this way it can provide considerable physical insight, and requires less computational effort than a full quantum calculation. Therefore, it is suitable for the treatment of multidimensional systems. In the following we give a brief outline of the Wigner formalism and show how it can be applied to the simulation of time resolved pump-probe signals. This derivation utilizes the method of Martens *et al.*[27]

The Hamiltonian of a molecular system represented in terms of adiabatic electronic states coupled to an electromagnetic field $\epsilon(t)$ can be written as

$$\hat{H}=\hat{H}_{\mathrm{mol}}+\hat{H}_{\mathrm{int}}\equiv\sum_a |a\rangle\hat{h}_a(\mathbf{Q})\langle a|-\hat{\mu}(\mathbf{Q})\epsilon(t), \tag{1}$$

where $\hat{h}_a(\mathbf{Q})$ is the vibrational Hamiltonian of the adiabatic electronic state a, and $\mathbf{Q}$ denotes the collection of vibrational coordinates. In the Hamiltonian (1) we have assumed the dipole approximation and the dipole operator $\hat{\mu}(\mathbf{Q})$ is given by

$$\hat{\mu}(\mathbf{Q})=\sum_{a,b} |a\rangle\hat{\mu}_{ab}(\mathbf{Q})\langle b|+\mathrm{h.c.} \tag{2}$$

Let $A(\mathbf{Q},\mathbf{Q}',t)\equiv\langle\mathbf{Q}|\hat{A}(t)|\mathbf{Q}'\rangle$ denote the matrix elements of a quantum mechanical operator $\hat{A}(t)$ in real space representation. Introducing the center of mass coordinate $\mathbf{q}=(\mathbf{Q}+\mathbf{Q}')/2$ and the relative coordinate $\mathbf{s}=\mathbf{Q}-\mathbf{Q}'$, the Wigner transform $A(\mathbf{q},\mathbf{p},t)$ of the operator $\hat{A}(t)$ is defined as

$$A(\mathbf{q},\mathbf{p},t)=\frac{1}{2\pi\hbar}\int_{-\infty}^{\infty} d\mathbf{s}e^{-i\mathbf{ps}}A(\mathbf{q}-\mathbf{s}/2,\mathbf{q}+\mathbf{s}/2,t). \tag{3}$$

In the Wigner approach,[32] the dynamics of the system is characterized in terms of Wigner distributions $P_{ab}(\mathbf{q},\mathbf{p},t)$ which are defined as the Wigner transform of the vibrational density matrix elements $\varrho_{ab}(\mathbf{Q},\mathbf{Q}',t)\equiv\langle a|\langle\mathbf{Q}|\hat{\rho}(t)|\mathbf{Q}'\rangle|b\rangle$. From this definition, the physical meaning of the Wigner distributions is obvious: The diagonal elements $P_{aa}(\mathbf{q},\mathbf{p},t)$ are the occupation densities of the electronic state a whereas the off-diagonal elements $(a\neq b)$ determine the transition probabilities from the electronic state a to the state b.

The equation of motion for the Wigner distributions can be obtained by transforming the Liouville equation for the density operator $i\hbar\partial\hat{\varrho}/\partial t=[\hat{H},\hat{\varrho}]$. This yields

$$i\hbar\,\frac{\partial P_{ab}(\mathbf{q},\mathbf{p},t)}{\partial t}=h_a(\mathbf{q},\mathbf{p})\exp\left(\frac{\hbar}{2i}\,\overleftrightarrow{T}\right)P_{\mathrm{ab}}(\mathbf{q},\mathbf{p},t)$$
$$-P_{\mathrm{ab}}(\mathbf{q},\mathbf{p},t)\exp\left(\frac{\hbar}{2i}\,\overleftrightarrow{T}\right)h_b(\mathbf{q},\mathbf{p})$$
$$+\epsilon(t)\sum_{c}^{c\neq a}\,(\mu_{ac}P_{cb}(\mathbf{q},\mathbf{p},t)$$
$$-P_{ac}(\mathbf{q},\mathbf{p},t)\mu_{cb}), \tag{4}$$

where

$$\overleftrightarrow{T}=\frac{\overleftarrow{\partial}}{\partial q}\frac{\vec{\partial}}{\partial p}-\frac{\overleftarrow{\partial}}{\partial p}\frac{\vec{\partial}}{\partial q}, \tag{5}$$

and with the Condon approximation for the dipole matrix elements. Equation (4) represents the basis for the description of optical excitation processes within the framework of Wigner distributions. Due to the highly nonlinear derivatives with respect to coordinates and momenta, Eq. (4) is too complicated for practical calculations without introducing further approximations. This formalism allows for a systematic investigation of quantum corrections to the classical behaviour of the system. The ''classical limit'' is obtained by using a $\hbar$-expansion of the exponentials in Eq. (4) and restricting to the lowest order.

Concerning the coupling to the electromagnetic field, the assumption that the field is weak enough in intensity allows to expand the Wigner distribution in a perturbation series, which can be formally written as $P_{ab}=\Sigma_i P_{ab}^{(i)}$ where the subscript i indicates the order in the field. Then we obtain in the ''classical limit'' for the transition probabilities ($a\neq b$) the equation

$$i\hbar\,\frac{\partial P_{ab}^{(i)}(\mathbf{q},\mathbf{p},t)}{\partial t}=(h_a(\mathbf{q},\mathbf{p})-h_b(\mathbf{q},\mathbf{p}))P_{ab}^{(i)}(\mathbf{q},\mathbf{p},t)$$
$$+\epsilon(t)\sum_{c}^{c\neq a}\,(\mu_{ac}P_{cb}^{(i-1)}(\mathbf{q},\mathbf{p},t)$$
$$-P_{ac}^{(i-1)}(\mathbf{q},\mathbf{p},t)\mu_{cb}),\quad a\neq b, \tag{6}$$

and for the occupation densities ($a=b$)

$$i\hbar\,\frac{\partial P_{aa}^{(i)}(\mathbf{q},\mathbf{p},t)}{\partial t}=\frac{\hbar}{i}\left\{\frac{\partial h_a(\mathbf{q},\mathbf{p})}{\partial\mathbf{q}}\,\frac{\partial P_{aa}^{(i)}(\mathbf{q},\mathbf{p},t)}{\partial\mathbf{p}}\right.$$
$$\left.-\frac{\partial h_a(\mathbf{q},\mathbf{p})}{\partial\mathbf{p}}\,\frac{\partial P_{aa}^{(i)}(\mathbf{q},\mathbf{p},t)}{\partial\mathbf{q}}\right\}$$
$$+\epsilon(t)\sum_{c}^{c\neq a}\,(\mu_{ac}P_{ca}^{(i-1)}(\mathbf{q},\mathbf{p},t)$$
$$-P_{ac}^{(i-1)}(\mathbf{q},\mathbf{p},t)\mu_{ca}). \tag{7}$$

Assuming the initial conditions $P_{ab}^{(0)}(\mathbf{q},\mathbf{p},t=0)=P_{ab}^{(0)}(\mathbf{q},\mathbf{p})$ for the Wigner distributions, and $\mathbf{q}_a(t=0;\mathbf{q}_{a0})=\mathbf{q}_{a0}$ and $\mathbf{p}_a(t=0;\mathbf{p}_{a0})=\mathbf{p}_{a0}$ for coordinates and momenta, respectively, Eqs. (6) and (7) can be iteratively solved

$$P_{ab}^{(i)}(\Gamma,t)=\frac{1}{i\hbar}\int_0^t dt_1\,\exp\left[-\frac{i}{\hbar}\,V_{ab}(\Gamma)(t-t_1)\right]\epsilon(t_1)$$
$$\times\sum_{c}^{c\neq a}\,[\mu_{ac}P_{cb}^{(i-1)}(\Gamma,t_1)$$
$$-P_{ac}^{(i-1)}(\Gamma,t_1)\mu_{cb}],\quad a\neq b, \tag{8}$$

$$P_{aa}^{(i)}(\Gamma,t)=\frac{1}{i\hbar}\int d\Gamma_{a0}\int_0^t dt_2\,\delta(\Gamma-\Gamma_a(t-t_2;\Gamma_{a0}))$$
$$\times\epsilon(t_2)\sum_{d}^{d\neq a}\,[\mu_{ad}P_{da}^{(i-1)}(\Gamma_{a0},t_2)$$
$$-P_{ad}^{(i-1)}(\Gamma_{a0},t_2)\mu_{da}], \tag{9}$$

where the abbreviation $\Gamma=\{\mathbf{q},\mathbf{p}\}$ and the definition $\delta(\Gamma-\Gamma_a(t-t_2;\Gamma_{a0}))\equiv\delta(\mathbf{q}-\mathbf{q}_a(t-t_2;\mathbf{q}_{a0}))\,\delta(\mathbf{p}-\mathbf{p}_a(t-t_2;\mathbf{p}_{a0}))$ were introduced. The quantity $V_{ab}(\Gamma)\equiv h_a(\Gamma)-h_b(\Gamma)$ denotes the energy gap between the electronic states a and b. The final expression for the occupation densities P_{aa} of the electronic state a has been obtained by inserting Eq. (8) into (9):

$$P_{aa}^{(i)}(\Gamma,t)=\frac{1}{\hbar^2}\,\Re\int d\Gamma_{a0}\int_0^t dt_2\int_0^{t_2}dt_1\,\delta(\Gamma-\Gamma_a(t-t_2;\Gamma_{a0}))$$
$$\times\epsilon(t_2)\epsilon(t_1)\sum_{c,d}\,\mu_{ad}(\mu_{dc}P_{ca}^{(i-2)}(\Gamma_{a0},t_1)$$
$$-P_{dc}^{(i-2)}(\Gamma_{a0},t_1)\mu_{ca})$$
$$\times\exp\left[-\frac{i}{\hbar}\,V_{da}(\Gamma_{a0})(t_2-t_1)\right]. \tag{10}$$

Equation (10) allows the calculation of the optical spectra such as photodetachment or photoionization spectra.

For time resolved spectroscopy with ultrashort laser pulses, a further specification of the pulse by a Gaussian envelope $\epsilon(t)=\exp[-t^2/2\sigma^2]\cos\omega t$ centered around the laser frequency ω can be introduced in Eq. (10). The product of the laser pulses with durations σ can be approximated by

$$\epsilon(t_1)\epsilon(t_2)$$
$$=\exp\left(-\frac{t_1^2}{2\sigma^2}\right)\exp\left(-\frac{t_2^2}{2\sigma^2}\right)\cos\,\omega t_1\,\cos\,\omega t_2$$
$$=\exp\left(-\frac{(t_1-t_2)^2}{4\sigma^2}\right)\exp\left(-\frac{(t_1+t_2)^2}{4\sigma^2}\right)\cos\,\omega t_1\,\cos\,\omega t_2$$
$$\approx\exp\left(-\frac{t_2^2}{\sigma^2}\right)\exp\left(-\frac{(t_1-t_2)^2}{4\sigma^2}\right)\cos\,\omega t_1\,\cos\,\omega t_2$$
$$\equiv I(t_2)\exp\left(-\frac{(t_1-t_2)^2}{4\sigma^2}\right)\cos\,\omega t_1\,\cos\,\omega t_2. \tag{11}$$

Using the variable transformation

$$\tau_1=t-t_2 \tag{12}$$

$$\tau_\alpha=t_2-t_1, \tag{13}$$

in Eq. (11) and the rotating wave approximation, the density distribution of Eq. (10) takes the following from:

$$P_{aa}^{(i)}(\Gamma,t)=\frac{1}{\hbar^2}\int d\Gamma_{a0}\int_0^t d\tau_1\int_0^{t-\tau_1}d\tau_\alpha \times\delta(\Gamma-\Gamma_a(\tau_1;\Gamma_{a0}))I(t-\tau_1) \times\sum_{c,d}\mu_{ad}(\mu_{dc}P_{ca}^{(i-2)}(\Gamma_{a0},t-\tau_1-\tau_\alpha) -P_{dc}^{(i-2)}(\Gamma_{a0},t-\tau_1-\tau_\alpha))\mu_{ca}) \times\exp\left[-\frac{i}{\hbar}(\hbar\omega-V_{da}(\Gamma_{a0}))\tau_\alpha\right]\exp\left[-\frac{\tau_\alpha^2}{4\sigma^2}\right]. \tag{14}$$

In order to obtain the analytic expression we made use of the fact that the Gaussian ($\exp[-\tau_\alpha^2/4\sigma^2]$) in Eq. (14) is strongly localized for short pulse durations σ, thus the upper limit $t-\tau_1$ of the integration variable τ_α can be set up to infinity. This allows for an analytic integration of the exponential part of Eq. (14), which yields the Gaussian spectral distribution determined by the pulse duration σ, as can be seen from Eq. (15):

$$P_{aa}^{(i)}(\Gamma,t)=\frac{1}{\hbar^2}\int d\Gamma_{a0}\int_0^t d\tau_1\,\delta\Big(\Gamma-\Gamma_a(\tau_1;\Gamma_{a0})\Big) \times I(t-\tau_1)\sum_{c,d}\mu_{ad}\Big(\mu_{dc}P_{ca}^{(i-2)}(\Gamma_{a0},t-\tau_1) -P_{dc}^{(i-2)}(\Gamma_{a0},t-\tau_1)\mu_{ca}\Big) \times\exp\left[-\sigma^2\frac{(\hbar\omega-V_{da}(\Gamma_{a0}))^2}{\hbar^2}\right]. \tag{15}$$

Equation (15) allows us to calculate more general time resolved optical signals which are determined by the occupation density of the electronic states and are not limited to the first order fields (cf. Ref. 27).

Our simulations of the pump-probe spectra involve the three adiabatic ground electronic states of the Ag_3^-, Ag_3, and Ag_3^+ system, denoted as 0, 1, and 2, respectively. Assuming that the pump and the probe process are both of the first order in the fields, Eq. (15) can be applied only twice to calculate the occupation densities $P_{11}(\mathbf{q},\mathbf{p},t)$ and $P_{22}(\mathbf{q},\mathbf{p},t)$ of states 1 and 2, respectively. For the occupation of the cationic state $P_{22}(t)$ we then obtain

$$P_{22}(t)=\int d\mathbf{q}d\mathbf{p}P_{22}(\mathbf{q},\mathbf{p},t)\sim\int d\mathbf{q}_0d\mathbf{p}_0\int_0^t d\tau_2\int_0^{t-\tau_2}d\tau_1 \times\exp\left[-\sigma_{pr}^2\frac{[E_{pr}-V_{21}(\mathbf{q}_1(\tau_1;\mathbf{q}_0))]^2}{\hbar^2}\right] \times\exp\left[-\sigma_{pu}^2\frac{[E_{pu}-V_{10}(\mathbf{q}_0)]^2}{\hbar^2}\right]I_{pu}(t-\tau_1-\tau_2) \times I_{pr}(t-\tau_2-t_d)P_{00}(\mathbf{q}_0,\mathbf{p}_0), \tag{16}$$

where dipole matrix elements are assumed to be constant. The indices pu and pr indicate the corresponding parameters of the pump and the probe field, respectively, and t_d denotes the time delay. Since under experimental conditions the probe step consists of a two-photon ionization, we have replaced the single-photon energy $\hbar\omega$ of Eq. (15) by the pump and the probe energies, $E_{pu}=\hbar\omega_{pu}$ and $E_{pr}=2\hbar\omega_{pr}$, presupposing a nonresonant character of the two-photon probe ionization. The quantities V_{10} and V_{21} stand for the energy gaps between the corresponding states. From this expression, the transient photoionization signal can be calculated according to

$$S[t_d]=\lim_{t\to\infty}P_{22}(t)\sim\int d\mathbf{q}_0d\mathbf{p}_0\int_0^\infty d\tau_1 \times\exp\left\{-\frac{(\tau_1-t_d)^2}{\sigma_{pu}^2+\sigma_{pr}^2}\right\} \times\exp\left\{-\frac{\sigma_{pr}^2}{\hbar^2}[E_{pr}-V_{21}(\mathbf{q}_1(\tau_1;\mathbf{q}_0))]^2\right\} \times\exp\left\{-\frac{\sigma_{pu}^2}{\hbar^2}[E_{pu}-V_{10}(\mathbf{q}_0)]^2\right\}P_{00}(\mathbf{q}_0,\mathbf{p}_0), \tag{17}$$

where the integration over the pump-probe correlation function has been carried out explicitly:

$$\int_0^\infty dt_2 I_{pu}(t-\tau_1-\tau_2)I_{pr}(t-\tau_2-t_d) =\sqrt{\pi}\sqrt{\sigma_{pu}^2+\sigma_{pr}^2}\exp\left\{-\frac{(\tau_1-t_d)^2}{\sigma_{pu}^2+\sigma_{pr}^2}\right\}\tilde{\epsilon}_{pu}^{\,2}\tilde{\epsilon}_{pr}^{\,2}. \tag{18}$$

So far we have described the photoionization process under zero volt emitted photoelectrons corresponding to ZEKE conditions. In general the electron can carry away any amount of kinetic energy. Thus for the simulation of the transient photoionization signal the integrations of the populations of the anionic and cationic states over the entire range of possible excess energies E_0 and E_2 have to be carried out. This leads to the expression for the NENEPO signals. Thus we obtain instead of Eq. (17)

$$S[t_d]\sim\int d\mathbf{q}_0d\mathbf{p}_0\int_0^\infty d\tau_1\,\exp\left\{-\frac{(\tau_1-t_d)^2}{\sigma_{pu}^2+\sigma_{pr}^2}\right\}\int_0^\infty dE_2 \times\exp\left\{-\frac{\sigma_{pr}^2}{\hbar^2}[E_{pr}-V_{21}(\mathbf{q}_1(\tau_1;\mathbf{q}_0))-E_2]^2\right\} \times\int_0^\infty dE_0\,\exp\left\{-\frac{\sigma_{pu}^2}{\hbar^2}[E_{pu}-V_{10}(\mathbf{q}_0)-E_0]^2\right\} \times P_{00}(\mathbf{q}_0,\mathbf{p}_0). \tag{19}$$

From Eqs. (17) and (19) for the pump-probe photoionization signals the following picture emerges. At the beginning the molecule is prepared in the electronic ground state 0 where the corresponding Wigner distribution $P_{00}(\mathbf{q}_0,\mathbf{p}_0)$ is assumed to be known (initial condition). This initial phase space density is spectrally filtered during the pump process to state 1 by the third Gaussians of Eqs. (17) and (19), respectively. Subsequently the filtered ensemble propagates on

the first state and is spectrally filtered again during the delayed probe pulse into state 2. This is expressed by the second Gaussians in Eqs. (17) and (19). Note that the Gaussian form of spectra during the pump and probe process are a direct consequence of both the classical approximation given by Eq. (6) and the short time assumption expressed by Eq. (11). The final time resolution of the signal is determined by the pump-probe correlation function given by the first Gaussians in Eqs. (17) and (19).

III. POTENTIAL ENERGY SURFACES AND THEIR CHARACTERIZATION

The calculation of the three ground state potential energy surfaces (PES) of Ag_3^-, Ag_3, and Ag_3^+ were carried out using a relativistic one-electron effective core potential accounting for core-valence correlation (RECP-CVC) together with the atomic basis set which was developed for the investigation of structural properties of neutral and charged silver clusters.[28,29] The use of RECP-CVC allowed for the full CI treatment of the three- and two-electron systems Ag_3 and Ag_3^+, while for Ag_3^- the computationally less demanding CCSD(T) method has been used instead to determine the ground state PES.

As already known from previous work,[28,29] the global minima of the anionic, neutral, and cationic silver trimers assume linear, obtuse triangular, and equilateral triangle structures, respectively. The normal coordinates Q_s, Q_x, Q_y, (or their polar representations Q_s, Q_r, α) of the Ag_3^+, cation have been used to present the PESs. Q_s, Q_x, and Q_y correspond to the symmetric stretching, the bending, and the antisymmetric stretching coordinate, respectively. One-dimensional cuts of the energy surfaces for Ag_3^-, Ag_3, and Ag_3^+ are shown in Fig. 1, in a direction Q_r which interconnects the linear equilibrium geometry of the Ag_3^- anion ($Q_r = -2.73$ Å) and the obtuse triangular equilibrium geometry of the Ag_3 neutral ($Q_r = -0.22$ Å). Thus the Q_r coordinate represents the direction of the structural relaxation of the system after the pump excitation. The location of the minimum of the anion at $Q_r = -2.73$ Å corresponds to a saddle point on the potential surface of the neutral Ag_3. However, the characteristics of this point (i.e., a relative maximum of the potential curve) is not exhibited in Fig. 1, since the Q_s value is kept constant at the equilibrium value of the neutral $Q_s = 2.81$ Å. The vertical electron detachment energy is 2.45 eV for the linear equilibrium geometry of the anion. The vertical ionization energy covers a large range of energies from 6.67 eV for the linear geometry of the anion to 5.73 eV for the obtuse triangular geometry of the neutral, providing the basis for probing the structural relaxation process. The first electronically excited state ($^2A_1$) of the neutral Ag_3 exhibits a curve crossing with the ground electronic state at $Q_r = 0$. Nevertheless the $^2A_1$ state has not been considered in the present work, despite possible significant nonadiabatic effects on the nuclear dynamics in the vicinity of the curve crossing.

Figure 2 shows Q_x, Q_y contour plots of the three ground state PESs for two fixed values for the symmetric stretching mode at $Q_s = 2.73$ Å and $Q_s = 2.81$ Å, which correspond to the absolute minima of the anion and the neutral Ag_3, respectively. Panel (a) exhibits the region around the linear equilibrium configuration of the Ag_3^- anion. This region corresponds to the vicinity of the saddle point of the neutral, panel (b). Also panel (c) contains the PES of the neutral, but spans the entire range, in which the nuclear relaxation dynamics following the pump excitation takes place, covering the region near the linear configuration at $Q_x \approx 1.4$ Å, $Q_y \approx 2.5$ Å (saddle point) and the Jahn–Teller region around $Q_x = 0$, $Q_y = 0$ with the threefold degenerate minimum. Panel (d) shows a contour plot of the Ag_3^+ cation with a minimum at $Q_x = 0$, $Q_y = 0$.[28,29] Note that also in Fig. 2 the saddle points appear as minima as a consequence of the fixed Q_s value.

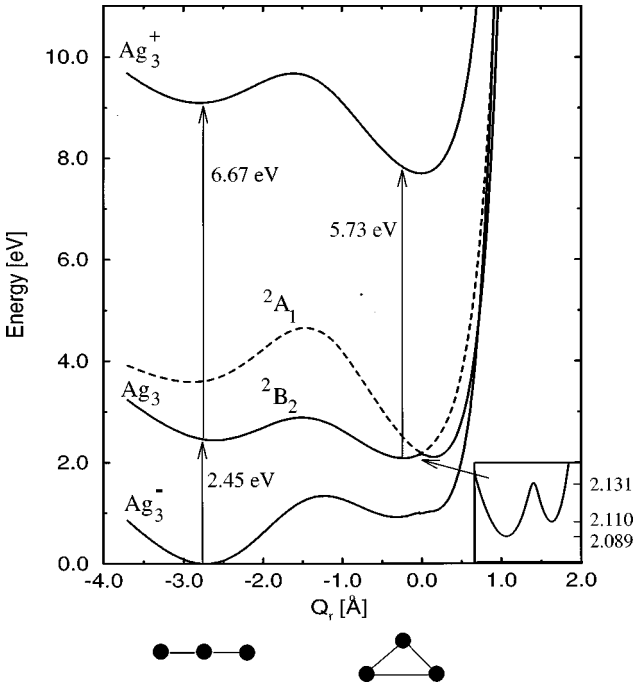

FIG. 1. One-dimensional cuts of the PES of the ground states for Ag_3^-, Ag_3, and Ag_3^+ along $Q_r = -(Q_x^2 + Q_y^2)^{1/2}$ for fixed values of the polar angle $\alpha = \arctan(Q_x/Q_y) = 120°$ and $Q_s = 2.81$ Å, which is the Q_s value of the equilibrium nuclear configuration of the neutral. The direction of the cut is also indicated in Fig. 2(c) as a diagonal line. The vertical electron detachment energy is VDE = 2.45 eV, the vertical ionization energy for the linear transition state and the equilibrium geometry of the neutral are 6.67 eV and 5.73 eV, respectively. The dashed line is the first electronically excited state of Ag_3.

Due to the linear geometry of the anion, the calculated PESs[33] had to be parameterized over a broad range in order to be used for molecular dynamics (MD) simulations. In this case the choice of coordinates is not trivial, since the regions of the PES with large repulsive interactions at short interatomic distances have to be considered. For this reason we have employed a set of curvilinear coordinates, which have the same symmetry properties as normal coordinates, but which allow us to represent the PESs efficiently by a larger density of grid points in the regions of the minima and valleys, and by a considerably lower density of grid points in the strongly repulsive regions. Making use of the permutation symmetry, the grid consists of $37 \times 82 \times 26$ points in the curvilinear coordinate system. The accuracy of the interpolation in the relevant parts of the PESs is $|E_{\mathrm{CI}} - E_{\mathrm{interpolated}}|$

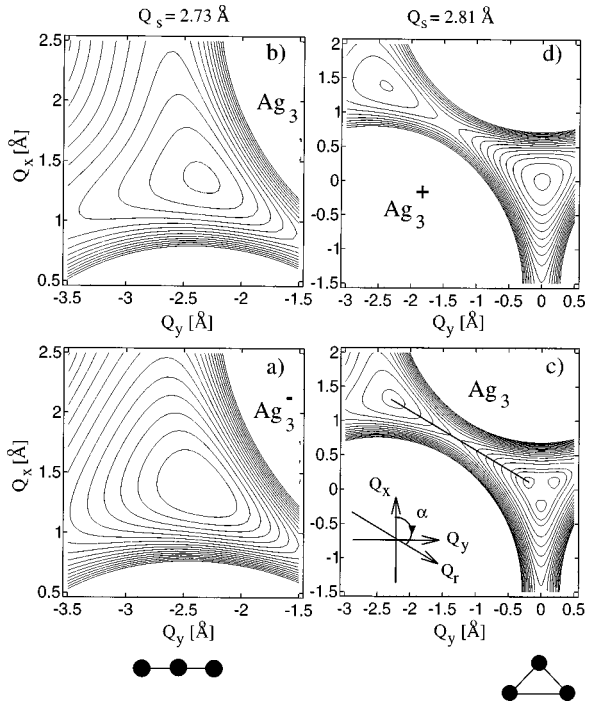

FIG. 2. Contour plots with respect to the Q_y (antisymmetric stretching) and Q_x (bending) coordinates of the ground state PESs for Ag_3^-, Ag_3, and Ag_3^+. The symmetric stretching coordinate (Q_s) is fixed at the equilibrium values for the anion $Q_s = 2.73$ Å (panels a,b) and for the neutral $Q_s = 2.81$ Å (panels c,d). In panel (c), the straight line connecting the saddle point of the linear configuration with the Jahn–Teller region of the obtuse triangle indicates the direction of the one-dimensional surface cut (cf. Fig. 1). The definition of the polar coordinate system is sketched in the lower left corner.

$\leqslant 10^{-5}$ a.u., with E_{CI} being the CI energy for the given nuclear configuration.

The dynamical properties of the equilibrated Ag_3^- anion and of the Ag_3 neutral at a given temperature were characterized from microcanonical long-time (64 ps) trajectories. Details of the MD simulations are presented in Sec. IV A.

Figure 3 shows the velocity autocorrelation Fourier transforms (power spectra) of the anion at 50 and 300 K, respectively. The three intense peaks are attributed to the harmonic vibrational frequencies at 30, 107, and 184 cm^{-1},

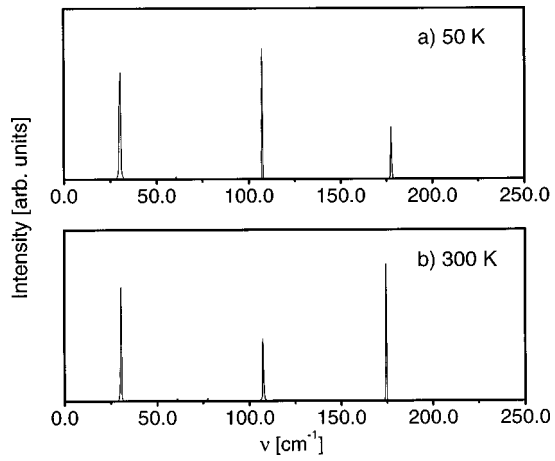

FIG. 3. The power spectra of Ag_3^- at 50 K and 300 K obtained from a long-time (64 ps) trajectory on the ground state hypersurface.

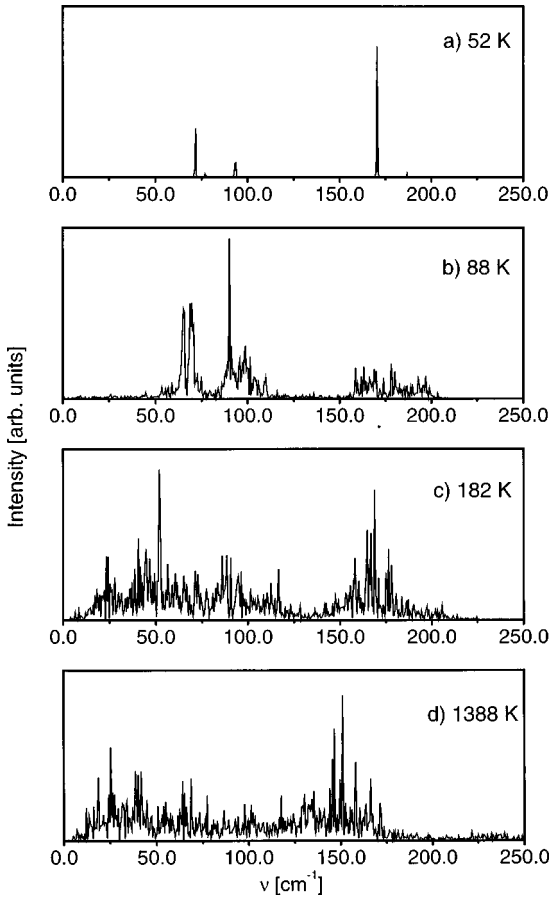

FIG. 4. The power spectra of Ag_3 at different temperatures. Each power spectrum was obtained from a single trajectory of 64 ps.

corresponding to the bending, the symmetric, and the antisymmetric stretching mode of the linear Ag_3^- ion. The deviations from harmonic behavior are small; the largest one has been obtained for the antisymmetric mode, whose frequency is lowered by 10 cm^{-1}. Additional peaks in the power spectrum induced by the anharmonicities are very weak.

The power spectra of the neutral Ag_3 (Fig. 4) are more complex and exhibit a substantially larger temperature dependence than those of the anion. The reason for this are large anharmonicities due to the Jahn–Teller distortion, leading to a threefold minimum of the ground state hypersurface with low energy barriers. The power spectra have been simulated up to 1400 K, which is the temperature range the neutral Ag_3 assumes after it relaxes from the pump excitation. The power spectrum at 52 K exhibits three relatively sharp peaks corresponding to the bending mode, the antisymmetric, and the symmetric stretching mode of the Ag_3 molecule. Comparison with harmonic vibrational frequencies of 73, 113, and 173 cm^{-1} indicates a particularly large deviation for the antisymmetric stretching mode. A pronounced line broadening and splitting has been already found at 88 K [cf. Fig. 4(b)].

Complementary to the power spectra at different temperatures, we have carried out a decomposition of the time-dependent kinetic energy into normal mode components at $T = 52$ and $T = 88$ K, in order to monitor the vibrational energy redistribution (IVR). This has been achieved by a linear

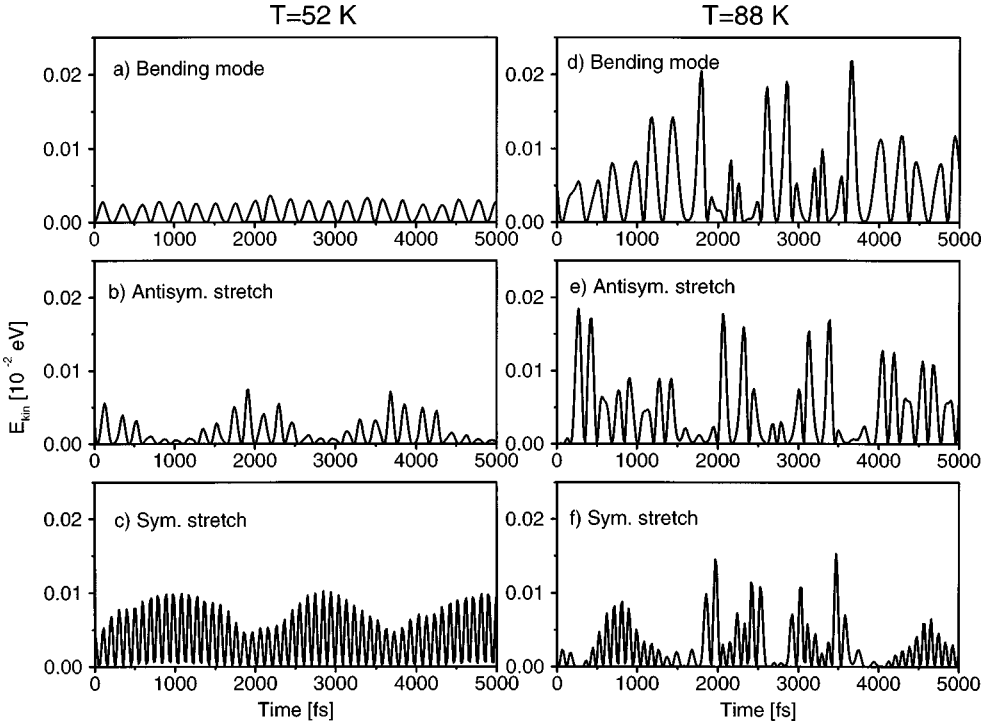

FIG. 5. The normal mode decomposition of the kinetic energy of Ag_3, carried out for the two single trajectories at 52 and 88 K.

transformation of the corresponding instantaneous velocities into the normal coordinates of the neutral Ag_3. Conservation of angular momentum requires the use of four coordinates with the rotational R_z mode (presuming that the nuclear motion takes place in the xy plane).

The normal mode decompositions of the kinetic energy at 52 and 88 K are shown in Fig. 5. The R_z component is omitted, since its kinetic energy is negligible. The kinetic energy in each mode exhibits an oscillatory behavior.[34] Pronounced beat effects are already present at 52 K, where in particular the symmetric and the antisymmetric stretch vibration exchange energy. At 88 K the IVR is so much enhanced that the oscillations exhibit highly irregular patterns.

The energy gap between the neutral and the cation PES is the central input quantity used to calculate the probe signal, as described in Sec. II. This quantity obtained in the course of a classical trajectory can also be used to calculate the line shape of the ionization spectrum.[35–37] Although this issue will be not addressed in this paper, it is instructive to consider the energy gap autocorrelation Fourier transform (''energy gap power spectrum''). It provides information on the subset of the vibrational spectrum contributing to Franck–Condon factors, i.e., which vibrational modes are active in the photoionization spectrum.[37] The energy gap power spectra shown in Fig. 6 illustrate that at low temperatures only the bending mode is active. At 1388 K (last panel of Fig. 6) additional intense low-frequency components are present, which are due to high-amplitude bending vibrations.

IV. NUCLEAR DYNAMICS OF THE NEUTRAL Ag_3 AFTER VERTICAL PHOTODETACHMENT

Within the Wigner approach presented in Sec. II, the simulation of pump-probe signals involves three steps: (i) generating a classical phase space density of the Ag_3^- anion in its ground electronic state at a given temperature; (ii) propagating this phase space density classically on the potential energy surface of the ground electronic state of the neutral Ag_3; and (iii) calculating the pump-probe NENEPO signals.

In this section we present a detailed analysis of the nuclear dynamics of Ag_3 after the vertical photodetachment, while in Sec. V we shall show how the nuclear dynamics is reflected in the simulated pump-probe signals. In the context of nuclear dynamics we shall provide an overall description and characterize the timescales of the sequential relaxation processes, which involve a linear-to-bent structural relaxation, an onset of IVR initiated by intracluster collisions, resonant, and dissipative IVR, and the completion of IVR. We shall also characterize the dependence of these timescales on the anion temperature.

A. MD simulations and initial conditions

We have performed simulations for vibrational temperatures of the Ag_3^- anion at 50 and 300 K. The phase space density of the equilibrated anion at each temperature is represented by an ensemble of both 1000 coordinates and momenta, which were sampled at regular time intervals of 10 fs from a microcanonical trajectory of 10 ps. The trajectories were generated by performing a classical MD simulation using the Verlet algorithm. Equilibration was achieved by an iterative rescaling of the velocities,[38] until the time-averaged kinetic energy was in correspondence to the desired temperature. The total angular momentum of the cluster was kept zero throughout the simulations. The temperature equilibration of Ag_3^- is expected to be a realistic description of the experimental conditions, where the anions are confined in an

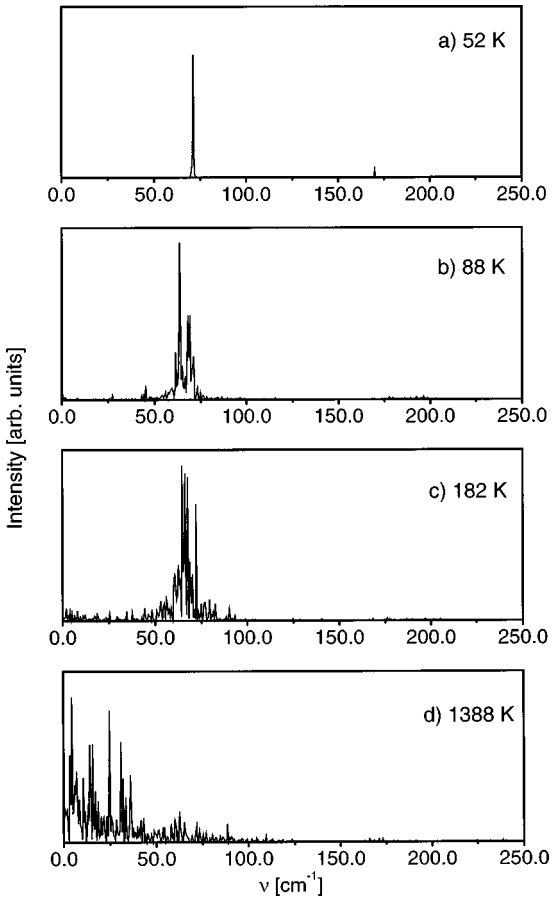

FIG. 6. The single-trajectory energy gap power spectra of the neutral Ag_3 at different temperatures.

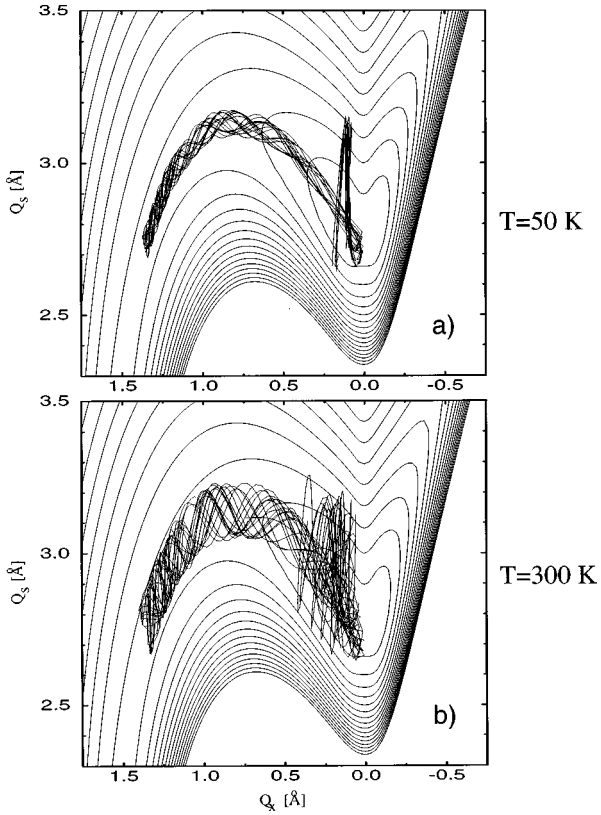

FIG. 7. Bunches of trajectories of the 50 and 300 K ensemble projected on a Q_x, Q_s contour plot of the potential energy surface of the neutral. Each bunch consists of 20 trajectories of 1.2 ps duration. The trajectories have been selected at random from the entire ensembles of 1000 trajectories.

ion trap and are thermalized by collisions with the buffer gas.[20] At each Ag_3^- temperature we have propagated 1000 trajectories on the PES of Ag_3, with the ensemble of 1000 sampled phase space points as the initial conditions.

B. Vibrational excess energy induced by the pump photodetachment

The vertical transition initiated by the pump pulse creates a phase space density on the ground electronic state PES of the Ag_3 neutral. The corresponding nuclear configuration is the linear geometry, being only slightly distorted by the thermal motions of the anion. Since the equilibrium geometry of the neutral is obtuse triangular, the molecule has a large vibrational excess energy and starts to relax. A vertical photodetachment from the equilibrium geometry of the anion leads to an excess energy of 0.357 eV on the hypersurface of the neutral, while the vibrational excess energy (averaged over 1000 trajectories) is 0.364 eV and 0.412 eV at 50 K and 300 K anion temperature, respectively. These temperatures 50 and 300 K correspond to a total kinetic energy of only 0.004 and 0.026 eV, respectively. Accordingly, the major part of the vibrational excess energy originates from the pump excitation rather than from the thermal energy of the anion.

C. Configurational relaxation, intracluster collision, and onset of IVR

Information on the dynamics of configurational relaxation and onset of IVR was obtained from bunches of trajectories of 1.2 ps projected on a contour plot (Q_s, Q_x, $Q_y=0$) of the neutral Ag_3 PES (Fig. 7). Q_s, Q_x, and Q_y, already introduced in Sec. III as the normal coordinates of the Ag_3^+ cation, also correspond to the symmetric stretch, the bending, and the antisymmetric stretching normal coordinates of the Ag_3 neutral. The time evolution of the system starts from the linear configuration around $Q_s=2.7$ Å and $Q_x=1.37$ Å on the Ag_3 PES, which is located in the flat region of the saddle point. With increasing time the system runs down the valley toward the potential minimum and becomes more bent. At the closest approach of the terminal atoms, which is located in the Jahn–Teller region around $Q_s=2.7$ Å and $Q_x=0.1$ Å, a strong repulsion sets in, resulting in the reflection of the terminal atoms. This reaching of the turning point on the PES corresponds to an intracluster collision. Up to the intracluster collision no significant IVR from the bending mode takes place. The intracluster collision induces a sharp reflection of the system from a motion across the Q_x bending coordinate to a motion along the Q_s stretching coordinate. From Fig. 7 and from visualizations of trajectories we infer that the intracluster collision triggers intense stretch vibrations. Accordingly, the intracluster collision manifests the onset of IVR. For initial temperatures of $T=50$ K [Fig. 7(a)] the ensemble remains spatially localized after the intracluster

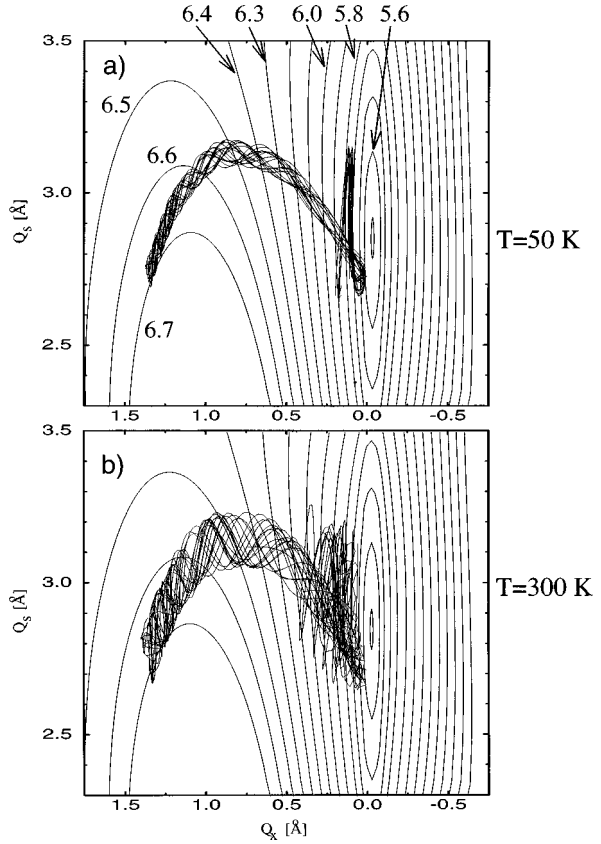

FIG. 8. Bunches of trajectories of the 50 and 300 K ensemble projected on a Q_x, Q_s contour plot of the cation-neutral energy gap surface. The values of the energy gaps in eV are indicated. The two bunches of 20 trajectories are identical with those already shown in Fig. 7.

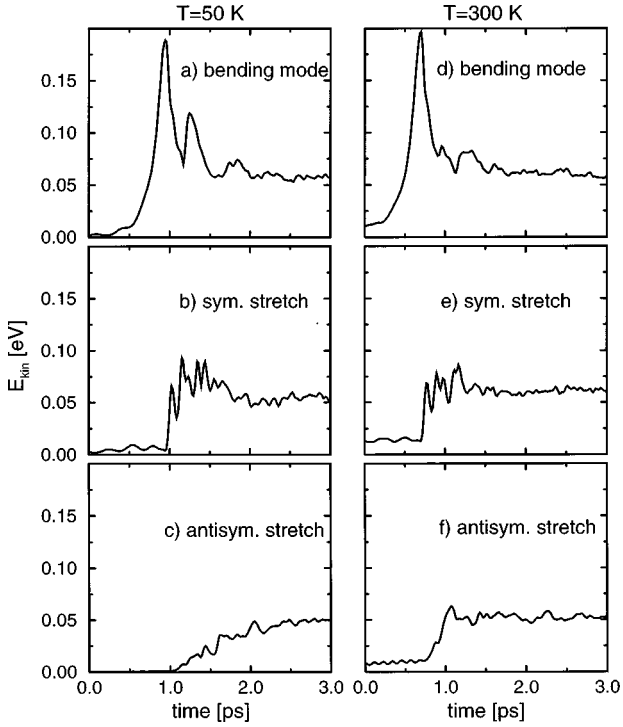

FIG. 9. The time evolution of the kinetic energy in the normal modes of Ag_3 following the pump excitation. The kinetic energies of the normal modes were obtained as averages over the entire ensembles of 1000 trajectories.

collision, in contrast to the 300 K initial ensemble [Fig. 7(b)]. This is a consequence of the fact that the intracluster collision enhances drastically the spatial spread of the trajectories which is more pronounced in the 300 K initial ensemble due to the larger thermal motions of the anion causing larger differences in the initial conditions.

It is instructive to project the same bunches of trajectories as in Fig. 7 on the cation-neutral energy gap hypersurface, since the latter determines the temporal shape of the pump-probe signals [$V_{21}(\mathbf{q}_1)$ in Eqs. (17) and (19)]. As depicted in Fig. 8, the contour lines of the energy gap between the cationic and the neutral Ag_3 are almost parallel to the symmetric stretching (Q_s) coordinate in the vicinity of the Jahn–Teller region. After the intracluster collisions at $Q_s = 2.7$ Å, $Q_x = 0.1$ Å the trajectories of the 50 K ensemble exhibit a concerted motion near the 5.80 eV contour line, manifesting spatial localization of the ensemble. This concerted motion has practically no component perpendicular to the contour line so that no energy gap oscillations occur. In the 300 K ensemble, the intracluster collision results in a spread of the trajectories, providing components perpendicular to the 5.80 eV contour line. This information will be significant for the elucidation of the pump-probe signals in Sec. V.

D. Timescales for configurational relaxation, onset, and evolution of IVR

Analysis of the time resolved dynamics in terms of normal modes provides central information on the timescales of distinct relaxation processes. The dynamics was described by considering the ensemble-averaged kinetic energy decomposed into the normal modes (Fig. 9) on the timescale of 3 ps after the pump excitation, for the $T = 50$ K and $T = 300$ K initial ensembles. The normal mode decomposition was carried out for each trajectory separately, cf. Sec. III, and then averaged over the entire ensemble of 1000 trajectories. At short times, the kinetic energy is very low in all modes, reflecting only the thermal motions of the initial ensembles. With increasing time the bond angle of Ag_3 decreases with the initial potential excess energy being converted into kinetic energy of the bending mode [cf. Fig. 9(a), (d)]. The maxima of the kinetic energy of the bending mode (when the kinetic energy in the stretching modes is still low) indicate that almost the entire kinetic energy is localized within the bending mode, while the ensemble attains a triangular configuration in the Jahn–Teller region (Fig. 8). The attainment of the maximum of the kinetic energy of the bending mode [Fig. 9(a), (d)], concurrently with the first passage through the Ag_3 Jahn–Teller region (Fig. 8), marks the lower limit for the intracluster collision time, since the subsequent drop of the kinetic energy is the consequence of running against the steep repulsive potential. The times $\tau_{\mathrm{COLL}}^{\mathrm{ON}}$ for the onset of collision obtained in this way are 950 fs for the 50 K and 710 fs for the 300 K ensemble. A more elaborate analysis of the collision time is presented in the Appendix, which gives similar values of $\tau_{\mathrm{COLL}}^{\mathrm{ON}} = 990$ fs for $T = 50$ K and $\tau_{\mathrm{COLL}}^{\mathrm{ON}}$

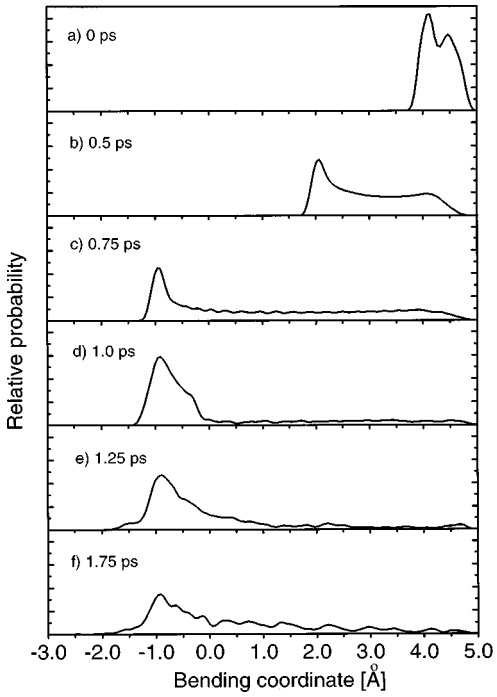

FIG. 10. Snapshots of the time evolution of the 300 K ensemble along the bending coordinate following the pump excitation. Each panel contains a histogram of the bending coordinate obtained from a normal mode decomposition of the instantaneous coordinates of the entire set of 1000 trajectories.

$=750$ fs for $T=300$ K. The intracluster collision induces a sudden transfer of the kinetic energy into the vibrational stretching modes, marking the onset of IVR. From the onsets of the rise of the kinetic energy of the symmetric stretching mode [Fig. 9(b), (e)] we infer the temporal onsets, $\tau_{\mathrm{IVR}}^{\mathrm{ON}}$, of IVR to be $\tau_{\mathrm{IVR}}^{\mathrm{ON}}=950$ fs for $T=50$ K and $\tau_{\mathrm{IVR}}^{\mathrm{ON}}=710$ fs for $T=300$ K. The close correspondence between the values of $\tau_{\mathrm{IVR}}^{\mathrm{ON}}$ and $\tau_{\mathrm{COLL}}^{\mathrm{ON}}$ confirms our picture of the instantaneous character of the process, i.e., IVR induced by an intracluster collision.

Complementary information on the nuclear dynamics can be obtained from a decomposition of the instantaneous coordinates into normal mode components. Figure 10 shows snapshots of the time evolution of the 300 K initial ensemble along the bending coordinate. Each snapshot of the time evolution is a histogram of the instantaneous bending mode expansion coefficients of the entire set of 1000 trajectories. Initially (i.e., at the instant of the pump excitation), the density of the bending mode is bimodal, reflecting the (classical) turning points of the bending vibration which originates from the thermal motion of the anion. Up to 750 fs, i.e., for $t \leqslant \tau_{\mathrm{COLL}}^{\mathrm{ON}}$, the density moves to lower values of the bending coordinate, according to the decrease of the bond angle. In addition, it acquires a long tail due to the initial velocity distribution in the bending mode. At 1.0 ps the density refocusses at low values (≈ -1 Å) of the bending coordinate, indicating a spatial localization of the ensemble in the Jahn–Teller region on the PES. At 1.25 ps the density becomes delocalized again as a consequence of IVR. The phase space density in the symmetric stretching mode (not shown) behaves similarly up to 750 fs, since a change of the bond angle corresponds to a linear combination of the bending and the symmetric stretching mode. In contrast, the antisymmetric stretching mode remains practically unchanged up to 750 fs. After 1.0 ps, when IVR dominates the dynamics, both stretching modes exhibit delocalization of densities.

Proceeding with the normal mode decomposition of the kinetic energy (Fig. 9) for longer times $t \geqslant \tau_{\mathrm{IVR}}^{\mathrm{ON}}$, we find signatures of resonant IVR for the 50 K ensemble. This is manifested by the second maximum of the kinetic energy in the bending mode at 1.2 ps, indicating that the kinetic energy flows partially back to the bending mode before being finally dissipated in the cluster. This fast and irreversible energy dissipation is induced by strong anharmonicities in the vicinity of the Jahn–Teller region.

The IVR process both at 50 and 300 K reveals sequential vibrational energy flow in the direction bending mode $\rightarrow$symmetric stretch$\rightarrow$antisymmetric stretch, R_z mode (Fig. 9). The excitation of the antisymmetric stretching mode (symmetry B_2), Fig. 9(c) and (f), is delayed relative to the symmetric stretching mode (A_1), which is of the same symmetry as the doorway bending mode (A_1), precluding resonant coupling between single quantum vibrational excitations of the different symmetry bending and antisymmetric stretching modes. The antisymmetric stretching mode is excited only in the Jahn–Teller region on the PES where a strong coupling of all modes occurs due to the anharmonicities. Note that a large elongation along the antisymmetric stretching coordinate corresponds to a pseudorotation leading to a reorientation of the the Ag_3 molecule in space.

At even longer times dissipative IVR results in vibrational equilibration. The IVR can be considered to be complete (i) when the energy is equally distributed among the modes, and (ii) when the oscillations of the kinetic energy are smoothed out, which means that the concerted character of the nuclear motion has been lost. According to these criteria, IVR is practically completed after $\tau_{\mathrm{IVR}}=2.0$–2.4 ps for the 50 K ensemble and after $\tau_{\mathrm{IVR}}=1.6$–1.8 ps for the 300 K ensemble (measured relative to the instant of the pump excitation)[39] as can be seen from Fig. 9. The larger τ_{IVR} value for the 50 K ensemble is mainly due to the smaller initial velocities, causing a delay of ≈ 250 fs during the structural relaxation compared to the 300 K ensemble. However, the IVR seems to have also a weak long-time component of at least 8 ps, which is manifested by a slight continuous increase of the kinetic energy in the R_z mode (not shown). Since our trajectories are limited to a temporal length of 8 ps, no information is currently available about the lifetime of this weak asymptotic tail. For long times $t \geqslant \tau_{\mathrm{IVR}}$ the kinetic energy is equally distributed (except from the possible weak asymptotic tail) among all the normal modes, indicating equilibration of the ensemble. The corresponding temperatures are 1300 and 1400 K for the initial temperatures 50 and 300 K, respectively.

In summary, both the 50 K and the 300 K initial ensemble reveal negligible IVR during structural relaxation from the linear to the triangular geometry at $t \leqslant \tau_{\mathrm{COLL}}^{\mathrm{ON}} \simeq \tau_{\mathrm{IVR}}^{\mathrm{ON}}$. The resonant IVR, which is more pronounced for the 50 K initial ensemble, is characterized by sequential

vibrational energy flow from the bending mode to the stretching modes, while dissipative IVR induces vibrational equilibration at longer times $t \geqslant \tau_{\mathrm{IVR}}$. The vibrational excess energies 0.364–0.412 eV result in final equilibrium temperatures of 1300–1400 K. It is instructive to note that dissipative IVR is exhibited already in a ''small'' three-atom system. We now proceed to confront the simulation results for the nuclear dynamics with the femtosecond pump-probe spectroscopy.

V. FEMTOSECOND PUMP-PROBE SIGNALS OF THE $Ag_3^- \rightarrow Ag_3 \rightarrow Ag_3^+$ SYSTEM

The original interpretation provided by Wolf *et al.*[20] of their experimental results of NENEPO pump-probe signals on the $Ag_3^-/Ag_3/Ag_3^+$ system was based on the assumption that the temporal shape of the signals is determined by the time-dependent changes in the Franck–Condon overlaps between the PES of Ag_3 and of Ag_3^+, during the relaxation process of Ag_3 along the bending coordinate, which corresponds to a structural change from the linear (equilibrium geometry of Ag_3^- and thus the initial configuration of Ag_3 after the vertical photodetachment) to the obtuse triangular geometry (equilibrium configuration of Ag_3). Lineberger *et al.*[26] invoked the additional effects of the acceleration of the nuclear wave packet of Ag_3 toward the triangular configuration with the maximization of the Franck–Condon factors between the PES of Ag_3 and Ag_3^+ in the vicinity of the triangular configurations. The rich dynamic information obtained in Sec. IV reveals that, in addition to the bending structural change, IVR processes play a dominant role in the dynamics for longer time delays. These involve the onset of IVR, resonant, and dissipative IVR and the final vibrational equilibration. This requires a more elaborate and complete interpretation of the NENEPO pump-probe spectra. In this section we show how the dynamics of Ag_3 is reflected in the simulated pump-probe signals of two different types: first, in the case of zero kinetic energy emitted photoelectrons, which corresponds to zero kinetic energy electron spectroscopy (NENEPO-ZEKE), and second, under the conditions of photoelectrons of arbitrary energy (NENEPO). The NENEPO experimental method,[20,26] which interrogates the total electron or ion yield, corresponds to the latter case. The calculation of the pump-probe NENEPO-ZEKE signal is performed using Eq. (17) while for the NENEPO signal we use Eq. (19).

A. Initial conditions for pump-probe signals

In order to study the pump-probe spectra of Ag_3^- at different initial temperatures (50 and 300 K), we have generated ensembles of initial conditions on the Ag_3 PES. These are characterized by the Franck–Condon transition probabilities in terms of the abundance of vertical electron detachment energies (VDEs) between the potential surfaces of Ag_3 and Ag_3^-. The histograms of the VDEs for the two ensembles are shown in Fig. 11. For short laser pulses, where the nuclear motion is slow compared to the temporal length of the laser pulse (static limit[7]), the histograms can be identified with the line shapes of the photodetachment spectra. Due to the larger vibrational amplitudes, the distribution of VDEs is broader

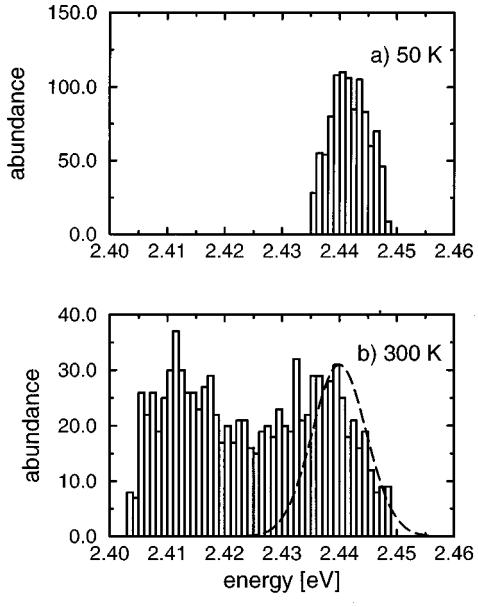

FIG. 11. Histograms of the vertical detachment energies (VDEs) of the Ag_3^- anion at (a) 50 and (b) 300 K, respectively. In order to demonstrate the spectral filtering, the line shape of a 100 fs Gaussian laser pulse at a pump energy of 2.44 eV has been inserted in panel (b).

for the 300 K ensemble. The asymmetric line broadening toward lower energies can be understood from the potential curves of the anion and of the neutral along the bending coordinate. Larger vibrational amplitudes lead to lower VDEs, while the maximum VDE at ≈ 2.45 eV corresponds to the equilibrium linear geometry of the anion and therefore constitutes a temperature-independent upper limit.

B. NENEPO-ZEKE pump-probe signals

We first present the calculated NENEPO-ZEKE signals for zero pump pulse durations ($\sigma_{pu}=0$). In this case the third exponential in Eq. (17) is equal to unity and therefore the spectral filtering (initial condition selection) due to the pump pulse is disregarded. Thus the entire anionic initial ensemble prepared at the given temperature is excited by the pump. Such probe simulations ($\sigma_{pu}=0$) enables us to obtain information on the effects induced by the pump and the probe pulse separately.

Figure 12 shows the simulated NENEPO-ZEKE probe signals for ensembles with 50 K and 300 K initial temperatures and for three different excitation energies, which correspond to: (i) $E_{pr}=6.50$ eV being close to the initial Franck–Condon transition (6.67 eV) and was chosen to interrogate the signal during the structural relaxation; (ii) $E_{pr}=5.8-5.9$ eV being close to the probing of the minimum of the neutral and was chosen for the interrogation of the characteristics of IVR; and (iii) an intermediate value of $E_{pr}=6.10$ eV. Moreover, two different Gaussian pulse durations were chosen, $\sigma_{pr}=100$ fs corresponding to the experimental conditions,[20,26] and a considerably shorter one, $\sigma_{pr}=20$ fs.

For the 50 K initial ensemble excited with 100 fs pulses [Fig. 12(a)], the onsets t_{INC} of the signals (''incubation times'') are 450, 700, and 750 fs for probe energies of 6.50, 6.10, and 5.80 eV, respectively. These incubation times for

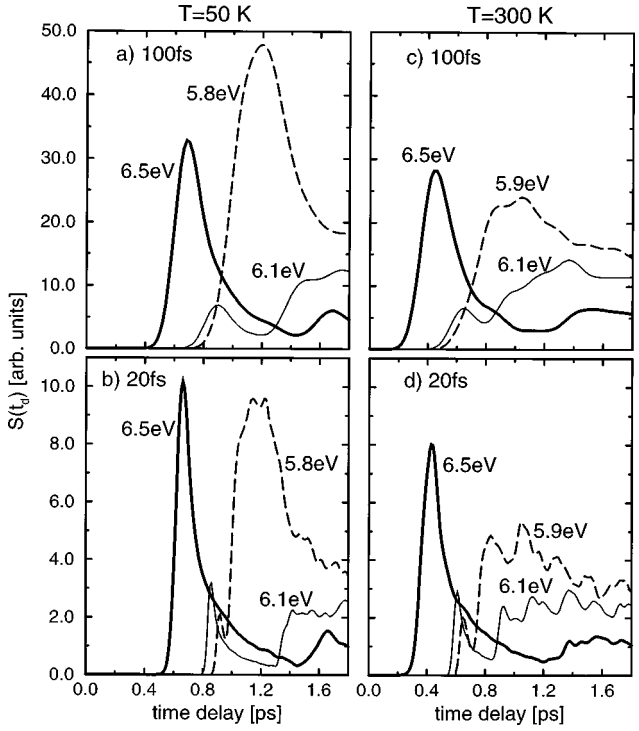

FIG. 12. The NENEPO-ZEKE probe signals ($\sigma_{pu}=0$) for the 50 K and 300 K initial ensemble, simulated for pulse durations σ_{pr} of 100 and 20 fs, and for energies E_{pr} of 5.80, 5.90, 6.10, and 6.50 eV.

all the probe energies are shorter than the onset of intracluster collisions and of IVR at this initial temperature. The decrease of t_{INC} with increasing E_{pr} reflects the earlier opening of the probe temporal window at higher probe energies, as the vertical ionization energy decreases from the linear (6.67 eV) to the triangular (5.73 eV) geometry (Fig. 1). The signals reach their first maximum at 700, 900, and 1200 fs for $E_{pr}=6.50$, 6.10, and 5.80 eV, respectively. Two situations can be distinguished: (i) $E_{pr}=6.50$ and 6.10 eV, where the signal maximum is reached during the structural relaxation prior to the onset of intracluster collision and of IVR. During the structural relaxation at $t\leqslant 900$ fs for the 50 K ensemble and at $t\leqslant 700$ fs for the 300 K ensemble, the front and the tail of the phase space density (as depicted in Fig. 10 for the 300 K ensemble) determines the temporal rise and fall of the signal, as is clearly manifested for $E_{pr}=6.50$ eV. The lower intensity of the signal at $E_{pr}=6.10$ eV arises from a larger spread of the phase space density at the longer delay time. Furthermore, the decrease of the signal after its maximum occurs already in the time domain of IVR. (ii) $E_{pr}=5.80$ eV, when the first maximum of the signal occurs in the temporal domain of IVR. This pronounced broad peak with high signal intensity [Fig. 12(a)] can be rationalized by the bunches of trajectories on the contour plots of the cation-neutral energy gap hypersurface [Fig. 8(a)]. After the intracluster collision at $T=50$ K the concerted character of the nuclear motion is preserved on the timescale of 900–1100 fs, with the system moving along the 5.80 eV contour line and exhibiting almost a constant vertical ionization potential.

The onsets (incubation times) of the signals at 300 K [cf. Fig. 12(c)] occur earlier (at $\approx$200–250 fs) than for the 50 K ensemble. Similarly, the peak of the signal for $E_{pr}=6.50$ eV exhibited at 400 fs ($<\tau_{\mathrm{IVR}}^{\mathrm{ON}}$) is shifted by 200 fs toward earlier time compared to the 50 K ensemble. This reflects a faster structural relaxation due to the higher initial kinetic energy in the bending mode. For time delays larger than 750 fs, the signals are dominated by IVR. In contrast to the 50 K initial ensemble, the $T=300$ K signal is strongly reduced in intensity at $E_{pr}=5.90$ eV. The different behavior of the 50 and 300 K ensembles in the IVR time domain is rationalized in terms of the contour plots on the cation-neutral hypersurface (Fig. 8), which reveal that the trajectories of the $T=300$ K ensemble exhibits a marked spatial spread after the intracluster collision [Fig. 8(b)], precluding a high accumulation of signal intensity as for the 5.80 eV signal of the $T=50$ K initial ensemble. The intracluster collisions of the $T=300$ K ensemble notably excite the Q_x and Q_y modes, resulting in energy gap oscillations, which constitute a necessary but by no means sufficient criterion for the observation of vibrational coherence.

The simulated signals with shorter pulse durations of $\sigma_{pr}=20$ fs [Fig. 12(b),(d)] allow us to gain insight into the details of the nuclear dynamics since the temporal resolution is enhanced in this case. For the 300 K initial ensemble, in the IVR regime the signals reveal oscillatory features [Fig. 12(d)] at probe energies of 6.10 and 5.90 eV indicating the signature of vibrational coherence induced by intracluster collisions. In contrast, the 50 K initial ensemble does not show a marked vibrational coherence. This counterintuitive result can be explained by invoking the two necessary conditions for the manifestation of vibrational coherence, (i) energy gap oscillations and (ii) a sufficiently concerted motion of the trajectories to preclude smearing out vibrational coherence effects by ensemble averaging. Condition (i) is not satisfied for the dynamics at $T=50$ K in the IVR time domain, as is evident from the dynamics projected on the energy gap hypersurfaces [Fig. 8(a)]. Accordingly, the intracluster collision does not induce vibrational coherence at $T=50$ K in accord with the pump-probe simulations [Fig. 12(b)]. The physical situation is different at $T=300$ K where also condition (i) is satisfied [see Fig. 8(b)]. From the simulated signals [Fig. 12(d)] at $E_{pr}=5.90$ and 6.10 eV, which reveal vibrational coherence, we infer that condition (ii) is also obeyed. Attempting to analyze the vibrational coherence of the 300 K ensemble, we note that the temporal spacing of the peaks is not equidistant and lies in the range of 100–150 fs. The quantum beat pattern of the ensemble-averaged signal [Fig. 12(d)] is another manifestation of the strong participation of the stretching modes, in addition to the results of the foregoing normal mode decomposition and Q_s, Q_x representations of the trajectories [Fig. 8(b)]. Specifically, the temporal spacing of 100–150 fs in the ensemble-averaged signal is consistent with the participation of the stretching modes (harmonic vibrational periods of the symmetric and antisymmetric stretching mode, being 193 and 295 fs, respectively), while the vibrational period of the bending mode (460 fs) is too long.

The long-time behavior (up to 7.5 ps) of the simulated NENEPO-ZEKE signals (Fig. 13) shows that the signals remain practically constant for $t\geqslant t_L$, where $t_L\simeq 2.0$–2.5 ps

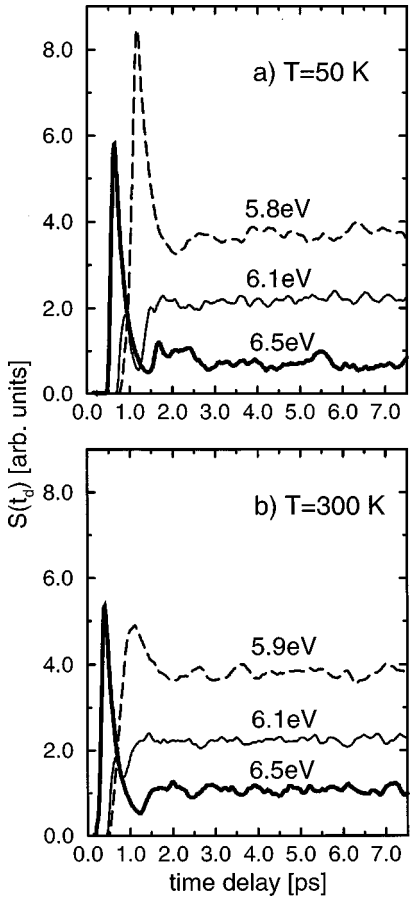

FIG. 13. The long-time NENEPO-ZEKE probe signals ($\sigma_{pu}=0$) for the 50 and 300 K initial ensemble, simulated for $\sigma_{pr}=100$ fs laser pulses up to a pump-probe delay time of 7.5 ps.

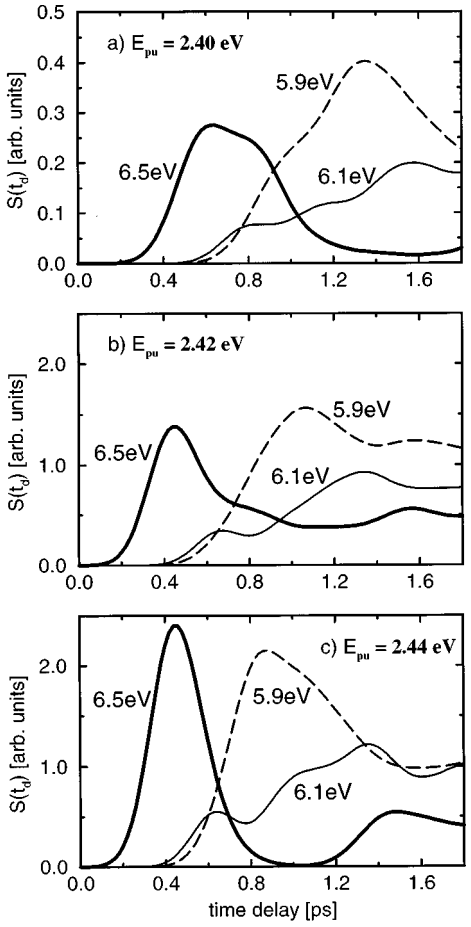

FIG. 14. The simulated NENEPO-ZEKE pump-probe signals for the 300 K initial ensemble with pump and probe pulses of 100 fs duration and excitation energies of the pump pulse of (a) $E_{pu}=2.40$ eV, (b) 2.42 eV, and (c) 2.44 eV. The excitation energies of the probe pulse are indicated at the signals.

for the $T=50$ K and t_L, where $t_L \simeq 1.5-2.0$ ps for the $T=300$ K initial ensemble. These times t_L manifest the completion of intracluster IVR, being in good agreement with the IVR times $\tau_{\mathrm{IVR}}=2.0-2.4$ ps for $T=50$ K and $\tau_{\mathrm{IVR}}=1.6-1.8$ ps for $T=300$ K, obtained in Sec. IV.

We turn to the incorporation of the pump step. The effect of the spectral filtering of the initial phase space density was investigated for pump energies of $E_{pu}=2.40$, 2.42, and 2.44 eV and a pulse width of $\sigma_{pu}=100$ fs, which has a Gaussian spectral width (FWHM) of 0.011 eV. To illustrate spectral filtering on the histograms of the vertical detachment energies (VDEs, Fig. 11), we have added in Fig. 11(b) the line shape of the 100 fs pulse centered at 2.44 eV. The overlap of the laser spectral line shape of the VDE histogram determines the weighting factors for the initial conditions. At 50 K, the spectral width of the laser can cover the entire histogram, so that we cannot expect a notable spectral filtering. For the 300 K ensemble the simulated NENEPO-ZEKE pump-probe signals (Fig. 14) reveal that the temporal shape of the signal at the pump energy of 2.44 eV agrees quite well with that of the probe signal [$\sigma_{pu}=0$, Fig. 12(c)]. With decreasing the pump energy to 2.42 and 2.40 eV signal intensity is shifted more toward later delay times. Lower VDEs correspond to larger vibrational elongations and thus to smaller initial kinetic energies in the bending mode. Therefore, initial conditions with low velocity components assume higher weights at lower E_{pu}. The generally lower absolute intensities at $E_{pu}=2.40$ eV are due to the smaller overlap of the spectral line shape of the laser with the VDE histogram.

C. NENEPO signals

Figure 15 illustrates the effect of the continuum states of the emitted photoelectron on the simulated probe NENEPO signal ($\sigma_{pu}=0$). These NENEPO signals reveal the following characteristics. (i) The onsets (incubation times) of the NENEPO and of the NENEPO-ZEKE signals are identical (Figs. 15 and 12), providing the same information about probing during the structural relaxation. (ii) The NENEPO signals are much broader, with the broadening growing with increasing probe energy, since all the energies below E_{pr} contribute to the signal. (iii) At high probe energies ($E_{pr}=6.1-6.5$ eV) the excessive broadening precludes the separation between structural relaxation and IVR in the NENEPO signals, in marked contrast to the corresponding NENEPO-ZEKE signals. (iv) At lower probe energies ($E_{pr}=5.8-5.9$ eV), for which the signal is dominated by IVR, the long-time saturation of the NENEPO signal, which marks the completion of IVR, is identical to the NENEPO-ZEKE signal. (v) The signatures of vibrational coherence of the 300

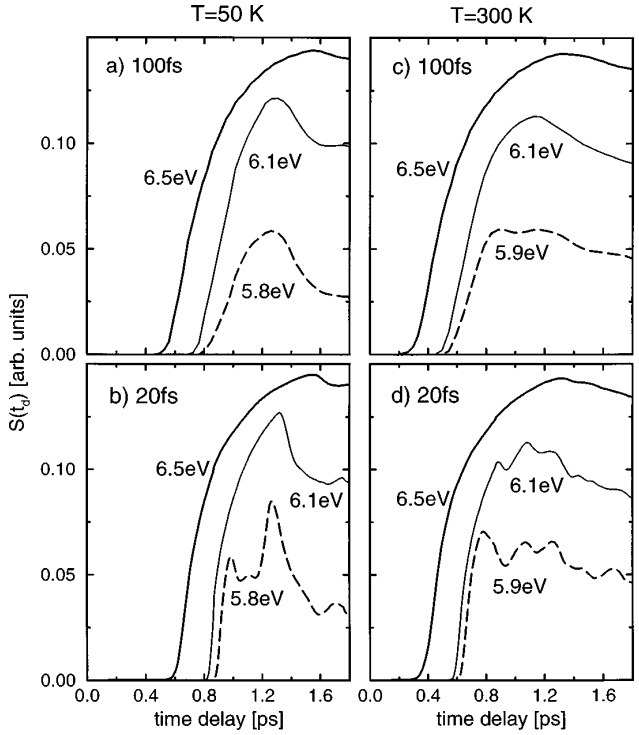

FIG. 15. The NENEPO probe signals ($\sigma_{pu}=0$) for the 50 K and 300 K initial ensemble, simulated for pulse durations of $\sigma_{pr}=100$ fs and $\sigma_{pr}=20$ fs and excitation energies E_{pr} of 5.80, 5.90, 6.10, and 6.50 eV.

K ensemble are conserved at lower probe energies. In general, the incorporation of the continuum states leads to the NENEPO signal broadening and to loss of information.

Figure 16 shows a comparison of the calculated photoionization signal of the 300 K initial ensemble with the experiment.[20] Obviously, the maxima of the signals are well reproduced by the simulations. Deviations are found for small time delays where the experimental results show an earlier onset of the signals, which may be due to direct multiphoton ionization by the pump pulse from the anion Ag_3^- to the cation Ag_3^+. A more detailed comparison between theory and experiment will be presented in the next section.

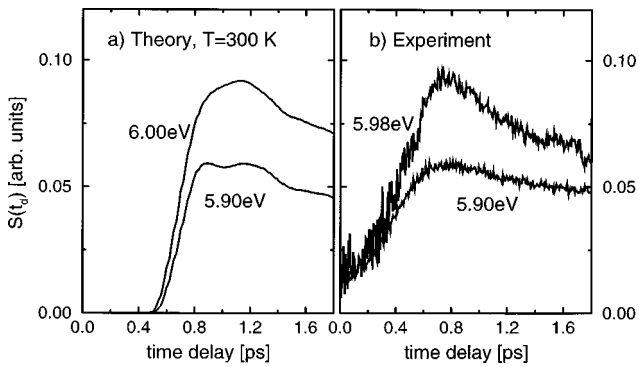

FIG. 16. A comparison between simulated and experimental NENEPO signals of Wolf *et al.* (cf. Ref. 20) for excitation energies of the probe pulse of 5.9 eV and 6.0 eV.

VI. CONCLUDING REMARKS

We explored intracluster dynamics in a small finite system on the timescale of nuclear motion. We focused on the microscopic description of the nuclear dynamics of Ag_3 on its ground electronic state potential surface, with the initial nonequilibrium linear $^2\Sigma_u^+$ state relaxing to the equilibrium $^2B_2$ configuration. The information emerging from our analysis falls into two related general categories. First, our MD simulations of the nuclear dynamics provided information on the structural relaxation dynamics of the nonequilibrium transition state of Ag_3, i.e., the nature of the nuclear relaxation process and their characteristic timescales. Second, the simulations of the femtosecond pump-probe spectroscopy using the semiclassical Wigner representation method for the density matrix results in a set of observables characterizing the time resolved signals (the electron or ion intensity versus the delay time between the pump and the probe pulse). The relation between these time-dependent observables and the characteristic time scales for the nuclear relaxation was established. Subsequently, we shall confront our simulated data with the experimental results,[20,26] inferring what is the information content of the NENEPO pump-probe femtosecond experiments and what new experimental and theoretical information is required.

Our analysis rests on the use of high-quality *ab initio* potential energy surfaces for classical molecular dynamics trajectory simulations, which were subsequently used for the Wigner representation of the density matrix for the calculation of the pump-probe signals. From the foregoing analysis it is apparent that meaningful theoretical information on energetics, Franck–Condon factors, and dynamics requires the use of accurate potential energy surfaces. The most straightforward relevant information pertains to the energetics of the ionization process (Fig. 1). The theoretical data for the vertical photodetachment energy (VDE) of Ag_3^- ($^1\Sigma_g^+$, VDE=2.45 eV), the vertical photoionization potential (VIP) of linear Ag_3 ($^2\Sigma_u^+$, $\mathrm{VIP_{lin}}=6.67$ eV) and of the triangular Ag_3 ($^2B_2$, $\mathrm{VIP_{triang}}=5.73$ eV) provides central information on the choice of the pump and the probe photon energies. Concurrently, the information for reliable Franck–Condon factors between realistic potential energy surfaces is significant. Regarding the pump process, the experimental data were obtained for $E_{pu}=2.95-3.13$ eV,[20,26] which considerably exceeds VDE=2.45 eV. On the basis of the information for the distribution of the Franck–Condon factors for the vertical photodetachment energies of Ag_3^- (Fig. 11) we inferred that in the energy range $E_{pu}=2.95-3.13$ eV the excess photon energy above the VDE is transferred to the kinetic energy of the ejected electron, while the initial vibrational distribution of Ag_3 is essentially determined by the thermally averaged vibrational overlap between Ag_3^- and Ag_3 (Fig. 11). Regarding the probe process, the energetics is limited by $\mathrm{VIP_{triang}} \leqslant E_{pr} \leqslant \mathrm{VIP_{lin}}$, characterizing the ionization probe detection window ($E_{pr}=5.73-6.67$ eV) for the interrogation of the dynamics from the linear to the bent structure of Ag_3. Finally, the time evolution of the configurational relaxation, i.e., the nature of the process and, in particular, the relevant timescales, require reliable potential energy surfaces.

Our analysis of the configurational changes in Ag_3 considered the initial linear configuration determined by the abundance of the coordinates and velocities for the Ag_3^- anion at a given temperature. Our simulations provided the following information for the nuclear dynamics.

(1) The initial time evolution across the bending coordinate on the time scale $0-\tau_{\mathrm{COLL}}^{\mathrm{ON}}$, where $\tau_{\mathrm{COLL}}^{\mathrm{ON}}$ is the intramolecular collision time.
(2) The intramolecular collision times are $\tau_{\mathrm{COLL}}^{\mathrm{ON}}=710$ fs for an anion temperature $T=300$ K and $\tau_{\mathrm{COLL}}^{\mathrm{ON}}=950$ fs for $T=50$ K. The decrease of $\tau_{\mathrm{COLL}}^{\mathrm{ON}}$ with increasing T reflects the higher initial velocities along the bending coordinate.
(3) The onset of IVR is manifested at $\tau_{\mathrm{IVR}}^{\mathrm{ON}}=710$ fs for $T=300$ K and at $\tau_{\mathrm{IVR}}^{\mathrm{ON}}=950$ fs for $T=50$ K. The $\tau_{\mathrm{IVR}}^{\mathrm{ON}}$ values coincide with the corresponding $\tau_{\mathrm{COLL}}^{\mathrm{ON}}$, clearly showing that IVR is induced by the intramolecular collision.
(4) The IVR process is sequential, i.e., bending mode→symmetric stretching mode→antisymmetric stretching mode. At the higher initial temperature ($T=300$ K) the pattern seems to be essentially dissipative, while at the lower initial temperature the pattern reveals some resonance effects.
(5) The IVR process is complete on the timescale $\tau_{\mathrm{IVR}}\sim 1.6$–$1.8$ ps for $T=300$ K and $\tau_{\mathrm{IVR}}\sim 2.0$–$2.4$ ps for $T=50$ K. The larger τ_{IVR} value at 50 K reflects that the time evolution of the lower temperature ensemble is generally delayed by ~ 250 fs due to the smaller initial velocities along the bending coordinate.

It is gratifying that the details of the nuclear dynamics of a small system at a finite temperature can be elucidated, distinguishing between sequential processes of configurational changes (along the bending coordinate), intramolecular collision, and IVR. The interrogation of these dynamic processes by pump-probe spectroscopy requires first the examination of the NENEPO-ZEKE photoelectron spectra for the two-photon ionization of Ag_3 (Figs. 12–14). The information emerging from the NENEPO-ZEKE signals can be quantified in terms of the following observables: (i) The incubation time t_{INC} for the onset of the signal. (ii) The time t_M for the maximum of the signal. (iii) The onset t_L of the long-time behavior of the signal, i.e., when the signal is smoothed down to a constant level.

In Fig. 17(a) we summarize the temporal observables together with the characteristic times obtained from the nuclear dynamics. From the NENEPO-ZEKE data we infer that

(1) The incubation times are all shorter than the collision times, i.e., $t_{\mathrm{INC}}\leqslant\tau_{\mathrm{COLL}}^{\mathrm{ON}}\simeq\tau_{\mathrm{IVR}}^{\mathrm{ON}}$. Accordingly, the incubation times (for all values of E_{pr}) probe the configurational change across the bending coordinate.
(2) The decrease of t_{INC} with increasing E_{pr} is due to the earlier arrival of the bending Ag_3 system to the probe time window.
(3) For high values of E_{pr} ($\simeq 6.5$ eV) with an early onset of the probe time window, the hierarchy of the timescales is $t_{\mathrm{INC}}\leqslant t_M\leqslant\tau_{\mathrm{COLL}}^{\mathrm{ON}}\simeq\tau_{\mathrm{IVR}}^{\mathrm{ON}}$. Under these circumstances a major part of the signal reflects dynamics prior to the intracluster collision, i.e., IVR-free dynamics. The NENEPO-ZEKE signal represents the time evolution of the configurational change across the bending coordinate. The temporal peak of the signal, t_M, corresponds to an obtuse triangular geometry with a bond angle of $\approx 120°$ as compared to 180° for the initial geometry of the Ag_3^- anion and 68° for the equilibrium geometry of the neutral Ag_3. The temporal rise and fall of the signal reflects the front and tail of the phase space density along the bending coordinate, respectively.
(4) For low values of E_{pr} (i.e., 5.8–6.0 eV) the value of t_M for the NENEPO-ZEKE signal is larger, so that the hierarchy of the timescales is $t_{\mathrm{INC}}\leqslant\tau_{\mathrm{COLL}}^{\mathrm{ON}}\leqslant t_M$. The probed dynamics until t_M is now much richer with the signal for $t_{\mathrm{INC}}\leqslant t\leqslant\tau_{\mathrm{COLL}}^{\mathrm{ON}}$ reflecting structural bending prior to IVR, while on the timescale $\tau_{\mathrm{COLL}}^{\mathrm{ON}}\leqslant t\leqslant t_M$ the IVR occurs.
(5) At low E_{pr} ($\leqslant 5.90$ eV), t_M for the NENEPO-ZEKE signal is in the range $\tau_{\mathrm{COLL}}^{\mathrm{ON}}\leqslant t_M\leqslant\tau_{\mathrm{IVR}}$.
(6) The time t_L, at which the NENEPO-ZEKE signal has smoothed down to its long-time constant level measures the IVR time, i.e., $t_L=\tau_{\mathrm{IVR}}$. Of course, t_L is nearly independent of E_{pr}.
(7) Spectral filtering. Under the condition that the pump energy is chosen in the range spanned by the photodetachment spectrum (histogram of VDEs, Fig. 11), which is 2.40–2.45 eV for $T=300$ K, some spectral filtering effects are exhibited. At the lower range of VDEs (≈ 2.40 eV) initial conditions with low kinetic energy in the bending mode are favoured. This leads to a shift of the NENEPO-ZEKE intensity profile toward later delay

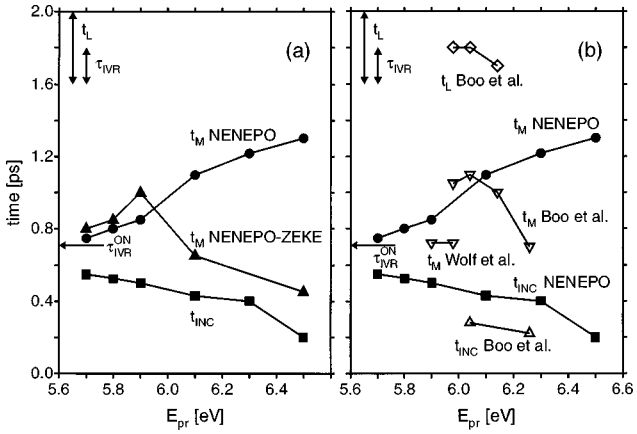

FIG. 17. A summary and comparison of the simulated and experimental characteristic timescales of dynamical processes in the neutral Ag_3 as a function of the probe energy (E_{pr}). (a) The simulated incubation times t_{INC}, the times t_M at which the signal assumes its maximum intensity, the time t_L at which the NENEPO and NENEPO-ZEKE signals reflect equilibration, the onset $\tau_{\mathrm{IVR}}^{\mathrm{ON}}$ and the completeness τ_{IVR} of IVR. Vertical arrows represent intervals of t_L and τ_{IVR} since they can be only approximately specified. (b) A comparison of the simulated NENEPO signals (filled symbols) with the experimental data (open symbols) of Wolf *et al.* (Ref. 20) and Boo *et al.* (Ref. 26). The data points in panels (a) and (b) are connected by straight lines to guide the eye.

times. The spectral filtering effect increases with increasing anion temperature.

The present experimental measurements of the NENEPO signals[20,26] involve the monitoring of the entire electron or positive ion yield, so that the NENEPO-ZEKE signals are integrated over the nearly constant density of continuum states of the emitted photo electron. Accordingly, details of the NENEPO-ZEKE signal are averaged out in part. The following features [Fig. 17(a)] of the NENEPO signals as compared to the NENEPO-ZEKE signals should be noted:

(1) The incubation times are practically identical for the NENEPO-ZEKE and for the NENEPO signals. Accordingly, features (1) and (2) of the t_{INC} for NENEPO-ZEKE signals hold also for the NENEPO signals, i.e., the incubation times of the NENEPO signals also increase with increasing E_{pr} and always preceed the intracluster collisions.
(2) There is a quantitative and qualitative difference between the t_M data and their E_{pr} dependence for the NENEPO and for the NENEPO-ZEKE signals. For high E_{pr} (≈ 6.50 eV) values the peak of the NENEPO signal is exhibited at considerably longer times than the corresponding NENEPO-ZEKE signal. Thus when configurational bending dynamics is solely probed, the accumulative continuum of the signal results in considerable information loss. Only for low values of E_{pr} (5.8–6.0 eV) the averaging effects on t_M are not pronounced.
(3) For larger E_{pr} the peak of the NENEPO signal is exhibited at $t_M \leqslant \tau_{\mathrm{IVR}}$, providing a lower limit for τ_{IVR}.
(4) The temporal onset t_L for the constant signal is practically equal for the NENEPO and for the NENEPO-ZEKE signals, providing a measurement for τ_{IVR}.
(5) The effect of the spectral filtering is smeared out, so that the temporal profile of the signal is nearly independent of E_{pu}.

Proceeding to the confrontation between our simulations and experiment,[20,26] we use the data for calculated NENEPO signals for the 300 K ensemble with the interrogating pulse length of 100 fs. The data extracted from the experimental signals have been summarized in Fig. 17(b) together with the simulated values.

(1) From the work of Boo *et al.*[26] two experimental incubation times are available for $E_{pr}=6.04$ eV and $E_{pr}=6.26$ eV. The incubation times are in the range 200–350 fs, which is in satisfactory agreement with our simulations. On the basis of this two data points it is not possible to recognize an E_{pr} dependence, in particular since the incubation time for $E_{pr}=6.04$ eV has a larger uncertainty. The signals of Wolf *et al.*[20] for probe energies of 5.90 and 6.00 eV (Fig. 16) exhibit no incubation times as the signals start rising immediately from the instant of the pump excitation. In general, signal intensity at zero delay time can arise from a direct multiphoton ionization of the anion by the pump pulse.
(2) The experimental data for the times t_M of the peak maxima do not form a consistent picture. While the two data points of Wolf *et al.*[20] are at ≈ 700 fs, three of the data points of Boo *et al.*[26] at 5.98–6.14 eV are at ≈ 1000 fs, and a further data point for $E_{pr}=6.26$ eV is at ≈ 700 fs. Our simulations predict an increase of t_M with increasing E_{pr}. This trend is not exhibited by the experimental data, although four out of six data points can be considered to be in satisfactory agreement with the simulated t_M values.
(3) The three experimental t_L values of Boo *et al.*[26] for $E_{pr}=5.98$, 6.04, and 6.14 eV are in the range 1.7–1.8 ps, being in good agreement with our simulations. For $E_{pr}=6.26$ eV the value signal decreases slowly up to ≈ 10 ps[26] and cannot be accounted for by our simulations.
(4) Our simulations predict an increase of the overall signal intensity with increasing E_{pr}. The signals of Boo *et al.*[26] at 5.98–6.26 eV show the reverse trend. The discrepancy between the simulated and the observed dependence of the signal intensity on E_{pr} observed by Boo *et al.*[26] may indicate the participation of one or more intermediate resonant electronic states, which take part in the two-photon ionization. At the present stage it is impossible to estimate qualitatively the influence of intermediate electronic states on the signal behavior.

From the foregoing analysis it is apparent that an extension of the experimental information will be desirable and interesting. We have assumed in the analysis of the experimental data the the Ag_3^- temperature is 300 K. NENEPO studies of Ag_3^- clusters over a broad temperature range will be of interest. The utilization of shorter ($\sigma_{pr}=20$ fs) pulses for interrogation will provide interesting information on vibrational coherence effects, predicted by us for $T=300$ K. Furthermore, the averaging process inherent in the calculation of the entire positive ion or total electron yield results in a considerable loss of information. The difficult femtosecond pump-probe experiment with detection of ZEKE electrons would be desirable. On the theoretical front, the extension of our treatment has to be extended in two directions. First, the description of the adiabatic dynamics used herein has to be extended to include nonadiabatic effects in the vicinity of the minimum of the bent structure, where the crossing of the potential surfaces $^2B_2$ and $^2A_1$ may require a more elaborate treatment. Second, our assumption of nonresonant two-photon probing may require extension at some probe energies where resonance effects due to the presence of intermediate states will be manifested. Such resonance effects are expected to modify both the intensity dependence on the probe energy as well as the time profile of the signal.

ACKNOWLEDGMENTS

We are indebted to Professor L. Wöste and Dr. T. Leisner for many stimulating discussions and for prepublication information. We are grateful to Professor W. C. Lineberger for providing us with a copy of his work (Ref. 26) prior to publication. This research was supported by the Deutsche

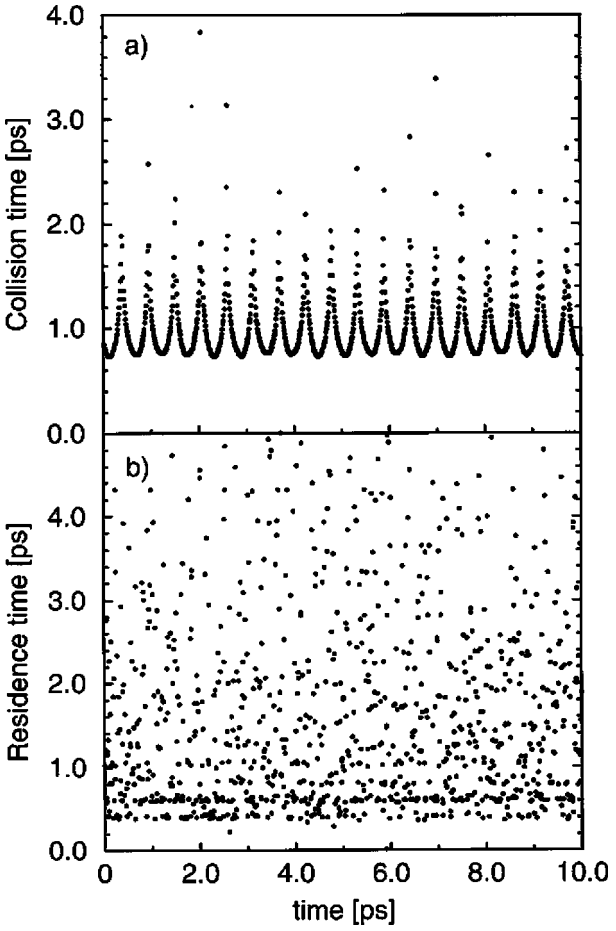

FIG. 18. The collision times (a) and residence times (b) of the 300 K ensemble versus the time of the anion trajectory, from which the corresponding initial condition of the trajectory was sampled.

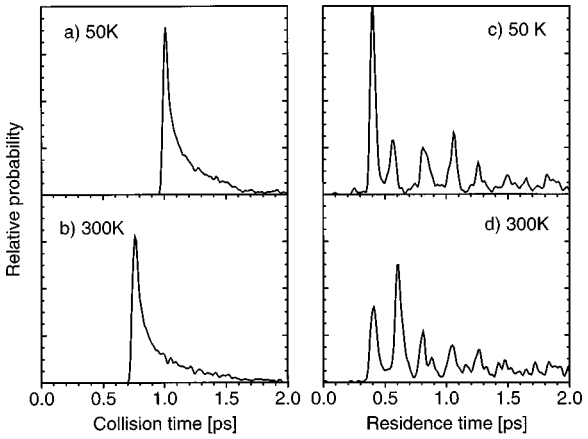

FIG. 19. Histograms of the collision times (a)–(b) of the 50 and 300 K ensemble and of the residence times (c)–(d) in the potential well around the equilibrium geometry of Ag_3. The collision times are measured relative to the time at which the pump excitation occurs, the residence times relative to the time of the collision instant of each trajectory.

Forschungsgemeinschaft SFB 337 and BO627/14-1 at Humboldt University, and by the Volkswagen Foundation at Tel Aviv University.

APPENDIX: ADDITIONAL DETAILS OF THE NUCLEAR DYNAMICS. COLLISION AND RESIDENCE TIMES

In Sec. IV we have analyzed the timescales for structural relaxation and intracluster collision, which induces IVR. For further characterization of the nuclear dynamics it is instructive to cross correlate the collision times for the single trajectories within the ensemble with the corresponding initial conditions of the trajectories. In Fig. 18(a) we plot the collision times of the single trajectories versus the corresponding initial conditions for the 300 K ensemble. The initial conditions of the 1000 trajectories were characterized by the times along the anion trajectory, from which the initial conditions were sampled at intervals of 10 fs. The collision time of a single trajectory was defined by the sharp characteristic minimum of the kinetic energy, which originates from a complete conversion of the kinetic energy of the bending mode into potential energy due to running against the steep repulsive potential. The collision times oscillate with a period of 550 fs, which is the oscillation period of the kinetic energy in the bending mode of Ag_3^-. (Note that the kinetic energy passes its maximum twice during the vibrational period.) This shows clearly that the collision times are correlated to the initial conditions of the trajectories. This is also the case for the 50 K initial ensemble.

In the next few hundred femtoseconds after the onset of the intracluster collision, the ensemble is mainly located in the potential well corresponding to the triangular configurations, with the vibrational excess energy being localized mainly in the stretching modes. However, the large vibrational excess energy can also flow back to the bending coordinate, leading to a partial escape of the ensemble from the potential well, as already inferred from the evolution of the density in the bending coordinate (Fig. 10). An analysis of the dynamics after the intracluster collision is provided in Fig. 18(b), where the residence times of the trajectories in the potential well are plotted versus the initial conditions. We defined the residence times as the period from the collision instant until the bond angle exceeds a value of 100°. In contrast to the collision times, the residence times are irregularly distributed clearly indicating that they are not correlated to the initial conditions.

Figure 19 displays histograms of the collision times and of the residence times. The distributions of the collision times are characterized by sharp onsets at $\tau_{\mathrm{COLL}}^{\mathrm{ON}}=990$ and 750 fs for the 50 and the 300 K ensembles, respectively [cf. Fig. 19(a),(b)]. They nearly coincide with the $\tau_{\mathrm{IVR}}^{\mathrm{ON}}$ values of 950 and 710 fs (Sec. IV D). The distribution of collision times has a monotoneously decreasing tail of 600–700 fs reflecting the configurational part of the phase space distribution along the bending mode (Fig. 10). In contrast, the distributions of residence times [Fig. 19(c),(d)] are multimodal, with the spacing of the main peaks about 200 fs, in accord with the vibrational period of the symmetric stretch vibration (harmonic vibrational period of 193 fs). This gives further support for a selective IVR between the bending and the symmetric stretching mode. The duration of the temporal ''progression'' of the residence times is about 1 ps. Note that the somewhat arbitrary definition for leaving the potential

well (exceeding the bond angle of 100°) influences only the onset of the temporal ''progression,'' but not the spacing.

It is self-evident from energetic considerations that the intense stretch vibrations induced by the intracluster collision are inherently connected to the Jahn–Teller region, i.e., to relatively small bond angles. Accordingly, the intense stretch vibrations terminate when the system runs back towards the saddle point in a partial (bond angles of, e.g., 100°) or complete (180°) back conversion from bent to linear configurations. Forth and back conversions are observed repeatedly in equilibrated systems, where upon every reentry into the Jahn–Teller region the intense stretch vibrations are recovered. The frequency of the escapes from the Jahn–Teller region is on the picosecond timescale, as can be inferred from the intense peaks below $30\,\mathrm{cm}^{-1}$ of the energy gap power spectrum at 1400 K, Fig. 6(d).

[1] A. H. Zewail, *Femtochemistry* (World Scientific, Singapore, 1994).
[2] *Femtosecond Chemistry*, edited by J. Manz and L. Wöste (VCH, Weinheim, 1995).
[3] *Femtochemistry*, edited by M. Chergui (World Scientific, Singapore, 1996).
[4] J. Jortner, in *Femtochemistry*, edited by M. Chergui (World Scientific, Singapore, 1996).
[5] J. Manz, ''Molecular Wave packet dynamics,'' in *Proceedings of the Nobel Symposium on Femtochemistry and Femtobiology* (Bjorkborn, Sweden, 1996—in press).
[6] J. Jortner, Z. Phys. D **24**, 247 (1992).
[7] S. Mukamel, *Principles of Nonlinear Optical Spectroscopy* (Oxford University Press, Oxford, 1995).
[8] J. Jortner, J. J. Chim. Phys. **92**, 205 (1995).
[9] J. Jortner and R. D. Levine, Isr. J. Chem. **30**, 207 (1990).
[10] D. Scharf, J. Jortner, and U. Landman, J. Chem. Phys. **88**, 4273 (1988).
[11] A. H. Zewail, Faraday Discuss. Chem. Soc. **91**, 207 (1991).
[12] A. Mokhtari, P. Cong, J. L. Herek, and A. H. Zewail, Nature (London) **348**, 225 (1990).
[13] M. Dantus, R. M. Bowman, M. Gruebele, and A. H. Zewail, J. Chem. Phys. **91**, 7437 (1989).
[14] A. Weaver, R. B. Metz, S. E. Bradforth, and D. M. Neumark, J. Chem. Phys. **93**, 5352 (1990).
[15] R. B. Metz and D. M. Neumark, J. Chem. Phys. **97**, 962 (1992).
[16] D. M. Neumark, Acc. Chem. Res. **26**, 33 (1993).
[17] S. M. Burnett, A. E. Stevens, C. S. Feigerle, and W. C. Lineberger, Chem. Phys. Lett. **100**, 124 (1983).
[18] K. M. Ervin, J. Ho, and W. C. Lineberger, J. Chem. Phys. **91**, 5974 (1989).
[19] P. G. Wenthold, D. Hrovat, W. T. Borden, and W. C. Lineberger, Science **272**, 1456 (1996).
[20] S. Wolf, G. Sommerer, S. Rutz, E. Schreiber, T. Leisner, L. Wöste, and R. S. Berry, Phys. Rev. Lett. **74**, 4177 (1995); R. S. Berry, V. Bonačić-Koutecký, J. Gaus, Th. Leisner, J. Manz, B. Reischl-Lenz, H. Ruppe, S. Rutz, E. Schreiber, S. Vajda, R. de Vivie-Riedle, S. Wolf, L. Wöste, Adv. Chem. Phys. **101**, 101 (1997).
[21] T. Leisner and L. Wöste (unpublished).
[22] H. O. Jeschke, M. E. Garcia, and K. H. Bennemann, J. Phys. B **29**, L545 (1996).
[23] H. O. Jeschke, M. E. Garcia, and K. H. Bennemann, Phys. Rev. A **54**, R4601 (1996).
[24] (a) M. Hartmann and V. Bonačić-Koutecký, presented at the Mixed Classical-Quantum Mechanical Systems Meeting, Dresden, October 1996; (b) A. Heidenreich, J. Jortner, M. Hartmann, J. Pittner, and V. Bonačić-Koutecký, presented at the James-Franck Symposium, Ein Gedi, January 1997; (c) M. Hartmann, A. Heidenreich, J. Pittner, V. Bonačić-Koutecký, and J. Jortner, presented at the Informal Cluster Workshop, Berlin, May 1997.
[25] O. Rubner, C. Meier, and V. Engel, J. Chem. Phys. **107**, 1066 (1997).
[26] D. W. Boo, Y. Ozaki, L. H. Andersen, and W. C. Lineberger, J. Phys. Chem. A **101**, 6688 (1997).
[27] Z. Li, J.-Y. Fang, and C. C. Martens, J. Chem. Phys. **104**, 6919 (1996).
[28] V. Bonačić-Koutecký, L. Cespiva, P. Fantucci, and J. Koutecký, J. Chem. Phys. **98**, 7981 (1993).
[29] V. Bonaić-Koutecký, L. Cespiva, P. Fantucci, J. Pittner, and J. Koutecký, J. Chem. Phys. **100**, 490 (1994).
[30] ''Mode Selectivity in Unimolecular Reactions,'' Special Issue, edited by J. Manz and C. S. Parmenter, Chem. Phys. **139**, 1 (1989).
[31] *Mode Selective Chemistry*, edited by J. Jortner, R. D. Levine, and R. B. Pullman (Kluwer, Dordrecht, 1991).
[32] M. Hillary, R. F. O'Connell, M. O. Scully, and E. P. Wigner, Phys. Rep. **106**, 121 (1984).
[33] The calculated ground electronic state PESs of Ag_3^-, Ag_3 and Ag_3^+ are available upon request.
[34] Although a partition of the potential energy is not possible because of cross terms, the total energy content in a given mode can be estimated, provided that the conversion between kinetic and potential energy in the mode is periodic. In this case, the envelope function spanned by the amplitudes of the oscillating kinetic energy function indicates the total energy content in the mode; A. Heidenreich, J. Jortner, and I. Oref, J. Chem. Phys. **97**, 197 (1992).
[35] L. E. Fried and S. Mukamel, Phys. Rev. Lett. **66**, 2340 (1991).
[36] L. E. Fried and S. Mukamel, J. Chem. Phys. **96**, 116 (1992).
[37] A. Heidenreich and J. Jortner, J. Chem. Phys. **105**, 8523 (1996), and references therein.
[38] D. Brown and J. H. R. Clarke, Mol. Phys. **51**, 1243 (1984).
[39] The antisymmetric streching mode contains somewhat less kinetic energy than the other two vibrational modes, since the R_z mode assums a small fraction of the kinetic energy to compensate the vibrational angular momentum.